

# Rarefaction-induced inflation and similarity breakdown of hypersonic bow shocks over a circular cylinder

Ehsan Roohi\*

Department of Mechanical and Industrial Engineering, University of Massachusetts Amherst,  
160 Governors Dr., Amherst, MA 01003, USA

Ahmad Shoja-Sani

Department of Mechanical Engineering, Ferdowsi University of Mashhad,  
Mashhad 9177948974, Iran

## Abstract

Rarefied hypersonic bow shocks over blunt bodies inflate as the Knudsen number increases, but it remains unclear whether this inflation is a simple shift and broadening of one common shock layer or a multi-scale change of the macroscopic and internal-energy fields. We address this question using direct simulation Monte Carlo (DSMC) data for Mach-10 flow over a circular cylinder in argon and nitrogen over  $Kn_\infty \approx 0.01-1$ , together with a Mach-number sweep at  $Kn_\infty = 0.01$ . At low rarefaction, a ray-based density-gradient ridge gives a reproducible bow-shock location and agrees with an independent schlieren-based shock-wave-detection method. As  $Kn_\infty$  increases, this ridge is replaced by a broad kinetic compression layer, so the high-Knudsen cases are analysed using profile-based standoff and thickness metrics rather than by imposing a visual shock line. The Knudsen- and Mach-number sweeps separate two mechanisms. At fixed  $M_\infty$ , the continuum normal-shock density ratio provides a useful low-rarefaction reference compression scale, whereas the measured standoff growth is governed primarily by the kinetic mean free path; the effective density thickness shows an intermediate minimum before increasing in the diffuse regime. At fixed low  $Kn_\infty$ , changing  $M_\infty$  mainly changes compression strength and curvature, preserving a coherent attached-layer structure. Density-registered profiles and shock-attached proper orthogonal decomposition (POD) show that, within the present maximum-density-gradient registration, density becomes nearly rank one, whereas Mach number and thermal variables retain independent modal content. Rarefied bow-shock inflation is therefore a coupled compression-relaxation process, not a single-scale rescaling of a continuum-like shock.

## 1 Introduction

Hypersonic flow over blunt bodies is governed by the coupled action of shock compression, boundary-layer development, surface accommodation and aerothermodynamic loading. When the molecular mean free path becomes comparable with the body length scale, the continuum approximation progressively loses validity and the bow shock can no longer be interpreted as a mathematical discontinuity. Instead, the compression region has a finite kinetic thickness whose location, width and internal relaxation structure depend on  $Kn_\infty$ , gas model and surface interaction. This rarefied regime is central to high-altitude flight, planetary entry, plume-body interaction and the validation of kinetic solvers. Direct simulation Monte Carlo (DSMC) remains the reference particle method for such flows [Bird, 1994, Cercignani, 2000, Roohi et al., 2025], while kinetic-theory and asymptotic analyses provide the complementary framework for interpreting slip,

---

\*Corresponding author: [roohie@umass.edu](mailto:roohie@umass.edu)

jump and high-Knudsen-number transport near solid bodies [Sone, 2007, Karniadakis et al., 2005, Sharipov and Kalempa, 2003, Sharipov, 2011].

Circular cylinders and spheres have long served as canonical blunt-body geometries in rarefied-gas dynamics because they contain a stagnation-line compression layer, a curved detached bow shock and strong gas–surface nonequilibrium in a geometrically simple configuration. For stationary cylinders, DSMC calculations by Stefanov et al. [2000] used the hypersonic circular-cylinder problem to study macroscopic fluctuations in rarefied flow fields, emphasizing that particle noise and statistical uncertainty are not merely numerical details but part of the diagnostic difficulty in extracting shock-layer quantities. The present test case is motivated by the continuum-breakdown study of Lofthouse et al. [2007], who compared computational fluid dynamics (CFD) and DSMC predictions for Mach-10 argon flow over a 12-in. circular cylinder and showed that gradient-length local Knudsen-number regions in the shock, boundary layer and wake can significantly affect aerothermodynamic quantities as the flow becomes more rarefied. In the slip and early transition regimes, Lofthouse et al. [2008] showed that velocity slip, temperature jump and non-equilibrium effects can strongly alter surface heating, force components and wake structure.

Hybrid particle–continuum simulations by Schwartzentruber et al. [2007] and related high-fidelity DSMC studies further demonstrate that rarefied hypersonic aerothermodynamics is governed by localized nonequilibrium and gas–surface interaction effects rather than by continuum shock relations alone. Related DSMC cylinder benchmarks were later used to validate new collision algorithms and hypersonic nonequilibrium simulations [Goshayeshi et al., 2015b,a]. More recent multiscale kinetic methods, including unified gas-kinetic scheme (UGKS) and unified gas-kinetic wave-particle method (UGKWP), have also used hypersonic cylinder cases as tests for all-regime rarefied-flow algorithms, including Mach-20 and Mach-30 cylinder problems spanning continuum and free-molecular limits [Huang et al., 2012, Zhu et al., 2019, Liu et al., 2020]. These studies establish the cylinder as a standard benchmark for force, heat-transfer and solver-validation questions, but they do not directly answer how the detached bow-shock layer itself loses single-scale similarity as rarefaction increases. Recent DSMC studies of wedge–cylinder shock–shock interaction over a wide Knudsen-number range similarly show that increasing rarefaction weakens the ability of the wave system to deflect and concentrate energy, altering heat-flux and skin-friction augmentation over the cylinder surface [Jiang et al., 2026]. These works motivate the present analysis, but their primary observables are force, heating, slip or interaction patterns, not the modal structure of the inflated bow-shock layer.

A second body of work has examined cylinders with rotation or moving surfaces, where rarefaction modifies the classical Magnus-effect picture and changes the balance of lift, drag and wall shear. Riabov [1999] investigated the aerodynamics of spinning cylinders in rarefied gas flows, and subsequent studies of high-speed rarefied flow past rotating cylinders reported inverse-Magnus behaviour and nonequilibrium force decomposition [John et al., 2016, 2018, 2019].

Shock detection is itself a separate issue in rarefied hypersonic flows. In continuum-like regimes, a schlieren or density-gradient edge gives a useful visual shock location. At larger  $Kn_\infty$ , however, the shock becomes a finite-thickness kinetic compression layer whose apparent centre depends on the diagnostic variable and on the extraction method. The shock-wave-detection (SWD) technique of Akhlaghi et al. [2017] provided a systematic way to identify shock centres and finite-thickness shock sides from numerical schlieren fields, and Akhlaghi et al. [2021] applied this idea to shock-polar analysis in rarefied flow over a circular cylinder. These methods are valuable for validating a shock-front extraction when a distinct edge exists, but they also highlight the limitation of representing transitional and free-molecular bow-shock layers by a single curve.

The present use of shock location and thickness measures should be interpreted in this operational sense. We do not seek a universal definition of a true shock surface or a universal shock thickness in the transitional and free-molecular regimes. Instead, the density-gradient location, gradient thickness and attached-coordinate maps are diagnostic quantities used to compare different macroscopic and internal-energy fields under the same registration procedure. The question is therefore not whether finite shock

thickness or rarefied relaxation exists in general, but whether a curved, detached hypersonic compression layer admits one common attached similarity coordinate for density, momentum and thermal variables.

This framing separates the present question from three neighbouring bodies of work. Classical rarefied-gas analyses and slip/jump studies, including the Boltzmann-based framework of Cercignani [2000], the molecular-gas-dynamics treatment of Sone [2007], and the gas–surface slip and jump data of Sharipov and Kalempa [2003], Sharipov [2011], provide the asymptotic framework for near-wall rarefied layers and boundary conditions, but they do not by themselves decide whether a detached, curved, external compression layer admits a single attached coordinate common to density and thermal variables. Hornung-type detached-shock and standoff scalings provide the appropriate continuum and near-continuum reference for the Mach sweep and for the low-  $Kn_\infty$  limit, but they do not determine the variable-dependent post-shock relaxation structure inside a finite rarefied layer. Existing DSMC cylinder benchmarks establish forces, heating, continuum breakdown and solver validation; the present analysis uses the same canonical geometry to ask a different question about selective compactness and similarity breakdown of the registered shock-layer fields.

Recent data-driven studies provide another motivation for revisiting the structure of rarefied cylinder flows. Neural-network and neural-operator surrogates can represent DSMC fields over Mach- and Knudsen-number sweeps, but their success depends on whether the underlying flow family has a compact low-dimensional structure [Roohi et al., 2026a,b]. In a related rarefied micro-nozzle problem, Roohi and Mahdavi [2026] showed that a nearly one-dimensional internal compression layer becomes highly compact after shock-centred registration: the leading density proper orthogonal decomposition (POD) mode increased from 83.33% of the fluctuation energy in physical coordinates to 98.33% in a jump-scaled coordinate, and a two-dimensional shock-window POD retained 99.05% of the energy in the first two modes. That result demonstrates that for a nominally one-dimensional compression layer, most of the apparent parametric complexity can be removed by locating the density-gradient station and scaling by the finite shock thickness. The present cylinder problem asks a more demanding question: whether the same shock-centred compactness survives for a curved, detached bow-shock layer with angular variation, wall curvature and gas-dependent thermal relaxation. Modal-analysis methods such as POD provide a direct way to measure this compactness: snapshots are arranged in a data matrix and decomposed by singular-value analysis, so that the cumulative energy quantifies the number of coherent structures needed to represent the parameter-induced variation [Lumley, 1967, Sirovich, 1987, Berkooz et al., 1993, Taira et al., 2017]. In contrast, dynamic mode decomposition targets time-shifted data and is used to identify growth rates and frequencies [Schmid, 2010, Rowley et al., 2009, Towne et al., 2018]; the present work instead uses POD as a parameter-space compactness diagnostic.

Modal analysis has also begun to enter kinetic and DSMC descriptions of hypersonic nonequilibrium flows. For example, Klothakis et al. [2021] combined DSMC base flows with linear stability analysis for hypersonic flat-plate boundary layers, while Senkardesler et al. [2025] used DSMC snapshots and dynamic mode decomposition to identify second-mode wave packets in a Mach-6 flat-plate boundary layer. In a shock-dominated configuration, Sawant et al. [2021] showed that rarefied hypersonic shock/boundary-layer interaction can sustain coherent global-instability structures not only in the separated region but also within the detached-shock layer. More recently, Karpuzcu et al. [2025] applied spectral proper orthogonal decomposition (SPOD) and dynamic mode decomposition (DMD) to DSMC-generated unsteady separated ramp flows and identified coherent shock-layer and shear-layer structures from stochastic kinetic snapshots. These studies motivate the use of modal tools for kinetic hypersonic data. In contrast to time-resolved SPOD/DMD analyses of unsteady disturbance fields, the present work uses POD as a parameter-space compactness diagnostic for shock-attached DSMC fields across Mach and Knudsen-number sweeps.

The unresolved question addressed here is therefore not whether rarefied hypersonic cylinder flows have been simulated before; they have. The question is whether the strong shock-centred collapse observed previously in an internal rarefied nozzle compression layer [Roohi and Mahdavi, 2026] extends to a geometrically more complex external bow-shock layer, or whether density, pressure, Mach number, translational

temperature and rotational temperature retain distinct shock-layer scales after registration. This distinction is important because many reduced-order descriptions and surrogate models implicitly assume that the dominant effect of rarefaction is a shift or broadening of a common layer. If density collapses but thermal and rotational fields remain multi-modal, then the inflated bow shock is not a simple geometrically rescaled shock but a multi-scale compression–relaxation structure.

The novelty of the present work is threefold. First, we validate a ray-based density-gradient shock extraction against the Akhlaghi et al. SWD method only in the low- $Kn_\infty$  regime where a distinct shock edge exists, and we do not impose a visual shock line in diffuse high- $Kn_\infty$  cases. Second, we extract quantitative profile-based standoff and thickness metrics from body-normal rays for both Knudsen- and Mach-number sweeps, so that high-Kn cases are treated as compression layers rather than discontinuities. Third, we use profile-level registration gain and shock-attached POD to show that, under the maximum-density-gradient registration used here, density compression becomes nearly rank one, whereas Mach number and thermal variables retain additional coherent structure. Thus the work connects classical rarefied cylinder aerothermodynamics, shock detection and modal compactness into a single framework for measuring the breakdown of single-scale bow-shock similarity.

This question is tested through three explicit hypotheses. First, if rarefaction-induced bow-shock inflation were mainly a geometric shift and broadening, density registration should remove most of the density variance ( $H_1$ ). Second, if the density-compression scale were universal, Mach number, pressure and the thermal/internal-energy fields should collapse with the same coordinate ( $H_2$ ); persistent modal content in those variables would instead indicate independent relaxation scales. Third, the Knudsen-number and Mach-number sweeps should have different compactness signatures if rarefaction changes the kinetic nature of the layer rather than only the inviscid compression strength ( $H_3$ ).

The contribution is not a new DSMC validation of hypersonic cylinder flow, nor a surrogate-modelling study of the type considered in recent neural-network work on rarefied cylinder data. Rather, this canonical configuration is used to test a specific fluid-mechanical hypothesis: whether rarefaction-induced bow-shock inflation can be represented by a single shock-attached coordinate common to density, momentum and thermal variables. The answer is selectively negative. The density field admits an almost rank-one registered representation, pressure follows the density coordinate more closely than the thermal variables, whereas Mach number and translational/rotational temperatures retain additional coherent modal content. This selective collapse is the central physical result: one-coordinate descriptions are useful for the density-compression layer but are not generally sufficient for nonequilibrium thermal/internal-energy fields. Rarefied bow-shock inflation is therefore a coupled compression–relaxation process rather than a geometric rescaling of a continuum-like shock layer.

The paper is organized as follows. Section 2 defines the DSMC data sets and the shock-attached scaling. Section 3 presents the results and discussion, including rarefaction-induced density inflation, Mach-number dependence, quantitative shock-layer metrics and POD compactness. Section 4 summarizes the main conclusions.

## 2 Problem definition and DSMC data

The configuration is a two-dimensional planar hypersonic flow over a circular cylinder of radius  $R$ . The incoming stream is aligned with the symmetry plane, and the upper half-plane is used for the analysis and visualization. The cylinder geometry is specified so that the leftmost point of the body is located at  $x = 0$ , giving  $x_c = R$  and  $y_c = 0$  for the cylinder centre. The freestream Knudsen number is defined using the cylinder diameter  $D = 2R$ ,

$$Kn_\infty = \frac{\lambda_\infty}{D}, \quad (1)$$

Table 1: Summary of the simulation and post-processing parameters used in the present analysis. The freestream density is varied consistently with the target  $Kn_\infty = \lambda_\infty/D$ ; all cases use the same cylinder diameter, wall condition, VHS gas model and ray-processing workflow.

Quantity	Value or definition
Geometry	Two-dimensional planar circular cylinder, $D = 0.3048$ m
Wall condition	Fully diffuse wall, $T_w = 500$ K
Freestream temperature	$T_\infty = 200$ K
Knudsen sweep	$M_\infty = 10$ , $Kn_\infty \approx 0.01$ –1
Mach sweep	$Kn_\infty = 0.01$ , $M_\infty = 5$ –15
Gases	Ar and $N_2$ , VHS collisions
Nitrogen internal energy	Rotational nonequilibrium in DS2V; no vibration/chemistry
Grid and particles	$194 \times 100$ divisions, about $1.5 \times 10^6$ simulator particles
Adaptive cells	Approximately 20 simulator particles per collision cell
Ray sector	$100^\circ \leq \theta \leq 180^\circ$ , 65 body-normal rays
Ray and attached grids	900 ray points; 260 points in $-1 \leq \xi_q \leq 4$
Main marker	Maximum radial density-gradient station for $\rho$ registration

where  $\lambda_\infty$  is the freestream mean free path associated with the corresponding DSMC inflow state. The primary Knudsen-number sweep is performed at  $M_\infty = 10$ , while an additional Mach-number sweep at  $Kn_\infty = 0.01$  is used to separate rarefaction effects from changes in shock strength. Both argon and nitrogen are considered, so that monatomic and rotationally relaxing gas responses can be compared. The geometry is a two-dimensional planar cylinder problem. All standoff, thickness and modal quantities therefore refer to this two-dimensional cylinder configuration.

The DSMC simulations were performed using Bird’s DS2V direct simulation Monte Carlo solver. The hypersonic cylinder case corresponds to a two-dimensional circular cylinder of diameter  $D = 0.3048$  m, freestream temperature  $T_\infty = 200$  K, and a fully diffuse cylinder wall held at  $T_w = 500$  K. Gas–gas collisions were modelled using the variable-hard-sphere (VHS) model. For argon, the molecular mass is  $m = 6.63 \times 10^{-26}$  kg, and the VHS reference parameters are  $T_{\text{ref}} = 273$  K,  $d_{\text{ref}} = 4.17 \times 10^{-10}$  m, and  $\omega = 0.81$ . For nitrogen, the molecular mass is  $m = 4.65 \times 10^{-26}$  kg, with the same reference temperature and reference diameter,  $T_{\text{ref}} = 273$  K and  $d_{\text{ref}} = 4.17 \times 10^{-10}$  m, and  $\omega = 0.74$ . The nitrogen calculations use the standard DS2V rotational nonequilibrium treatment for a diatomic gas; vibrational excitation and chemistry are not included in the benchmark fields used here. The computational domain was discretized using  $194 \times 100$  divisions, and approximately  $1.5 \times 10^6$  simulator particles were used. During the simulations, the collision cells were continuously adapted to maintain an average of about 20 particles per cell, providing adequate resolution of the collision statistics throughout the domain. The DSMC data and the corresponding cylinder benchmark were previously validated against Bird’s reference solution and related DSMC calculations [Goshayeshi et al., 2015b,a]. The present post-processing uses the time-averaged DS2V macroscopic fields. The solver and the underlying cylinder benchmark fields have already been validated in the cited DSMC studies; the additional checks in the present paper therefore target the extracted shock-layer metrics, registration procedure and modal conclusions rather than constituting a new solver-verification exercise. Independent block-averaged confidence intervals were not available for all cases, so the shock-layer extraction uses median upstream/downstream estimates, a fixed ray sector and comparative POD metrics to reduce sensitivity to local DSMC sampling scatter. The robustness analysis in Appendix A further varies the extraction settings to test whether the modal conclusions depend on reasonable post-processing choices.

The wall temperature is therefore higher than the freestream temperature ( $T_w/T_\infty = 2.5$ ), but it is still

below the translational temperature generated inside the hypersonic post-shock layer. The wall boundary condition should consequently be interpreted as a relatively warm diffuse wall compared with the incoming gas, but as a weaker thermal sink for the shock-heated gas than an isothermal wall held at  $T_\infty$ . This distinction is important for the interpretation of the thermal fields: the density-compression layer is mainly controlled by the incoming momentum flux and rarefaction, whereas the near-wall translational and rotational temperature fields are also influenced by the finite wall temperature and by gas–surface energy accommodation.

For clarity, the shock-attached notation used below is defined here. The radial distance from the cylinder centre is  $r$ , and  $s = r - R$  is the distance measured from the wall along a body-normal ray. The polar angle  $\theta$  is measured from the positive  $x$ -axis,  $q$  denotes a generic macroscopic field,  $q_{\text{up}}$  and  $q_{\text{down}}$  are robust upstream and downstream ray averages,  $r_q$  or  $s_q$  is the location of the maximum radial gradient of  $q$ ,  $\delta_q$  is the corresponding gradient-based thickness, and  $\xi_q$  is the variable-attached coordinate. The symbols  $E_i$  and  $C_i$  denote, respectively, the fractional POD energy of mode  $i$  and the cumulative energy through mode  $i$ . These definitions are repeated in the equations below when they enter the analysis.

## 2.1 Shock detection and validation

The present analysis requires a reproducible definition of the bow-shock location in DSMC fields where the compression layer has a finite kinetic thickness rather than a discontinuous jump. For cases in which a distinct edge exists, we define the shock centre as a density-gradient ridge and compare it with the schlieren-based shock-wave detection (SWD) method of Akhlaghi et al. [2017], later applied to rarefied shock polars over cylinders by Akhlaghi et al. [2021].

Let  $(x_c, y_c)$  and  $R$  denote the centre and radius of the circular cylinder. For each polar angle  $\theta$ , the DSMC field is sampled along the ray

$$\mathbf{x}(r; \theta) = (x_c, y_c) + r(\cos \theta, \sin \theta), \quad r > R. \quad (2)$$

The low- $Kn_\infty$  shock-centre radius is defined as the first significant upstream density-gradient peak outside a near-wall exclusion region,

$$r_s(\theta) = \arg \max_{r \in \mathcal{I}_s(\theta)} \left| \frac{\partial \rho}{\partial r}(\mathbf{x}(r; \theta)) \right|, \quad (3)$$

where  $\mathcal{I}_s$  is restricted to the upstream compression layer and excludes points too close to the cylinder surface. The corresponding local standoff distance is

$$\Delta_s(\theta) = r_s(\theta) - R. \quad (4)$$

For each macroscopic variable  $q$ , we define a variable-specific gradient thickness,

$$\delta_q(\theta) = \frac{|q_{\text{down}}(\theta) - q_{\text{up}}(\theta)|}{\max_{r \in \mathcal{I}_s(\theta)} |\partial q / \partial r|}, \quad (5)$$

where  $q_{\text{up}}$  and  $q_{\text{down}}$  are robust upstream and downstream averages along the same ray. The associated attached coordinate is

$$\xi_q = \frac{r - r_q}{\delta_q}, \quad (6)$$

where  $r_q$  is the location of the maximum radial gradient of  $q$ . This definition is used for density, Mach number, pressure, translational temperature and, for nitrogen, rotational temperature.

The ray extraction and registration were implemented with fixed numerical settings for all cases. The upstream shock sector was sampled with 65 uniformly spaced body-normal rays over  $100^\circ \leq \theta \leq 180^\circ$ , where  $180^\circ$  corresponds to the stagnation line in front of the cylinder. Each ray was sampled using 900

points from the wall to either the computational-domain boundary or  $8R$ , whichever was reached first. The scattered DSMC cell-centred data were evaluated on the ray by piecewise-linear interpolation over a Delaunay triangulation of the original  $(x, y)$  points. The profile was mildly smoothed only for locating the maximum-gradient station and the gradient thickness; the registered field values themselves were obtained from the normalized ray profile by one-dimensional linear interpolation onto the common grid  $-1 \leq \xi_q \leq 4$  with 260 points. Thus the POD is performed on the same attached grid for every snapshot, while the original invalid or unsupported regions remain masked.

The search interval  $\mathcal{I}_s(\theta)$  excludes the near-wall region  $s < 0.015R$  and the far end of the sampled ray  $s > 0.94s_{\max}$ , so that wall jumps and domain-boundary plateaux are not selected as shock-layer gradients. The downstream value  $q_{\text{down}}$  is the median of the smoothed profile between 3% and 23% of the valid ray length outside the wall, while  $q_{\text{up}}$  is the median over the farthest 15% of the valid ray. These median averages make the jump estimate insensitive to individual noisy DSMC cells. The precise numerical modal energies can depend weakly on the selected angular sector, attached-grid resolution and interpolation procedure. For this reason, the quoted energies are interpreted as diagnostics for the stated shock-attached representation rather than as universal constants. The central comparison is more robust than the individual numbers because all variables are processed with the same ray sector, interpolation, masking and POD procedure. Appendix A repeats the extraction with alternative angular sectors, ray numbers, attached-grid resolutions, smoothing widths and common-support thresholds.

The SWD comparison is used only as a validation in cases where a narrow schlieren-like edge is present. In the SWD method, the density field is first converted to a numerical schlieren image, and a Roberts-cross edge detector is then applied to obtain a local shock-response function. Along each local row or sampling direction, the response in the shock neighbourhood is approximated by a Gaussian profile,

$$G_i(x) = B_{1,i} \exp \left[ -\frac{(x - B_{2,i})^2}{2B_{3,i}^2} \right], \quad (7)$$

where  $i$  denotes the local sampling row,  $G_i(x)$  is the fitted schlieren-response profile,  $B_{1,i}$  is the peak response amplitude,  $B_{2,i}$  is the shock-centre location, and  $B_{3,i}$  is the Gaussian width parameter associated with the finite shock thickness. The normalized within-shock coordinate is then defined as

$$\sigma_i(x) = \frac{G_i(x)}{B_{1,i}}. \quad (8)$$

With this definition,  $\sigma_i = 1$  occurs at  $x = B_{2,i}$  and denotes the SWD shock centre, while lower values of  $\sigma_i$  identify locations away from the centre of the finite-thickness shock-response profile. In the present comparison,  $\sigma_i = 0.1$  is used to mark the aft or post-shock side of the fitted shock layer.

Figure 1 shows a representative validation case at  $Kn_\infty = 0.01$  and  $M_\infty = 10$ . The Akhlaghi et al. SWD shock-centre points agree closely with the ray-based density-gradient ridge, while the  $\sigma \simeq 0.1$  points lie on the downstream side of the finite-thickness shock layer. At larger Knudsen numbers, the bow shock becomes a broad kinetic compression layer rather than a narrow image edge; in that regime, the present work uses layer-based measures and does not impose a unique visual shock line.

## 3 Results and discussion

### 3.1 Rarefaction-induced bow-shock inflation

Figure 2 shows the density field for the Knudsen-number sweep at fixed  $M_\infty = 10$ . At  $Kn_\infty = 0.01$  and  $0.025$ , both gases exhibit a distinct bow-shock front, and the detected front is overlaid for reference. As  $Kn_\infty$

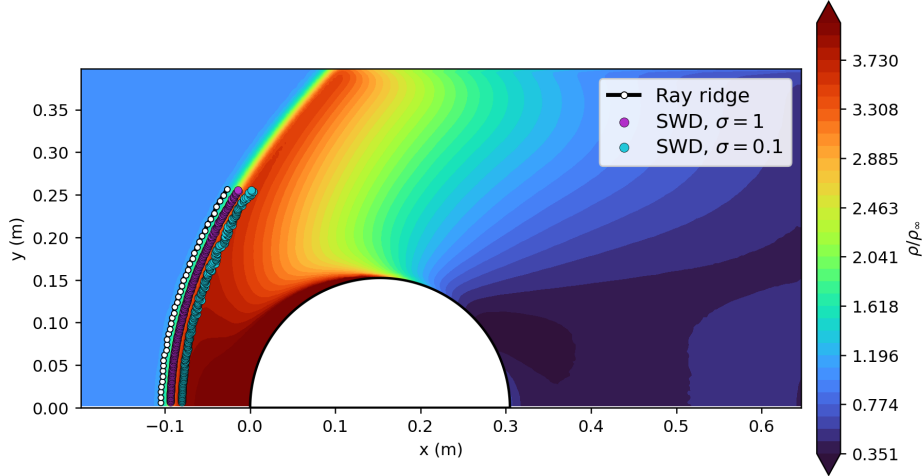


Figure 1: Validation of the low- $Kn_\infty$  shock-front extraction for the representative argon case at  $Kn_\infty = 0.01$  and  $M_\infty = 10$ . The black curve with white markers denotes the ray-based density-gradient ridge used in the present analysis. The purple points show the Akhlaghi et al. SWD shock-centre locations ( $\sigma = 1$ ), while the cyan points show the corresponding aft-shock locations ( $\sigma = 0.1$ ). The close agreement between the ray ridge and the SWD shock-centre points supports the use of the ray-based extraction in the low-rarefaction regime where a distinct shock edge exists.

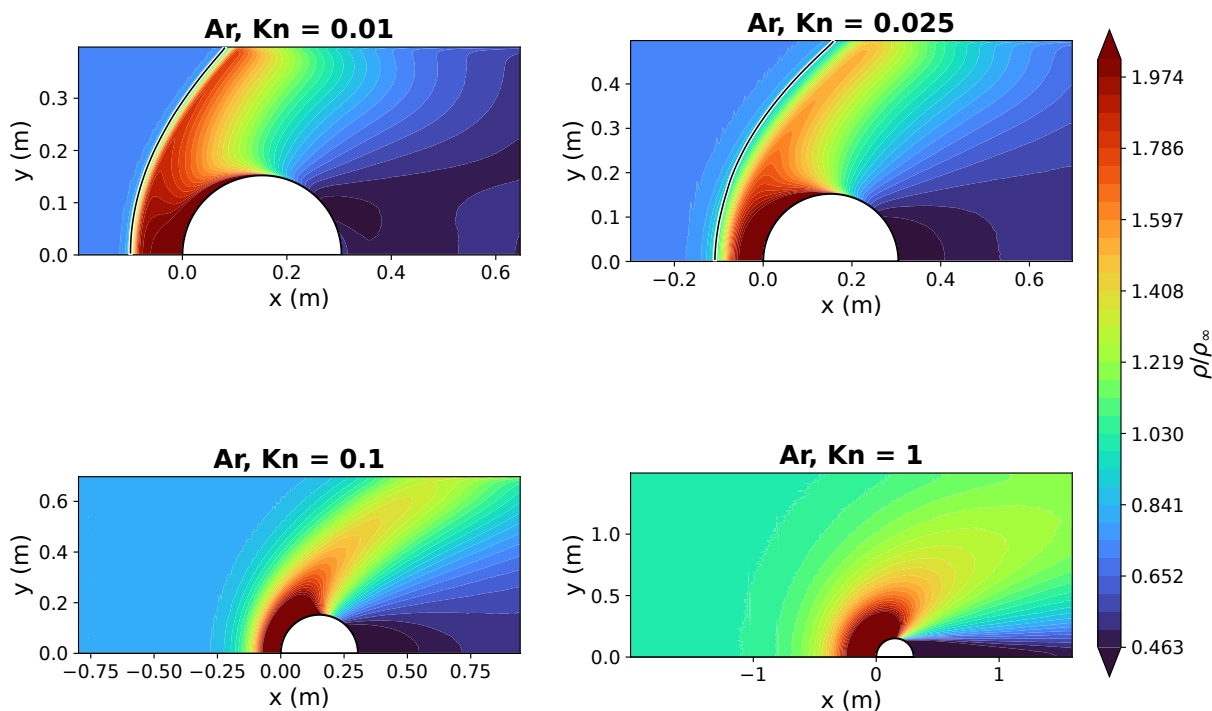
increases to 0.1 and 1, the sharp front is replaced by a spatially extended compression layer. The high- $Kn_\infty$  panels are therefore interpreted as shock-layer inflation rather than displacement of a single discontinuity.

The argon and nitrogen fields show the same qualitative progression: upstream broadening of the density-compression region, weakening of the sharp density ridge, and increased interaction between the compression layer and the near-body region. The similarity of the density fields indicates that rarefaction is the dominant control parameter for the gross inflation of the bow-shock layer, whereas differences between argon and nitrogen become more important in the thermal and internal-energy relaxation fields analysed below.

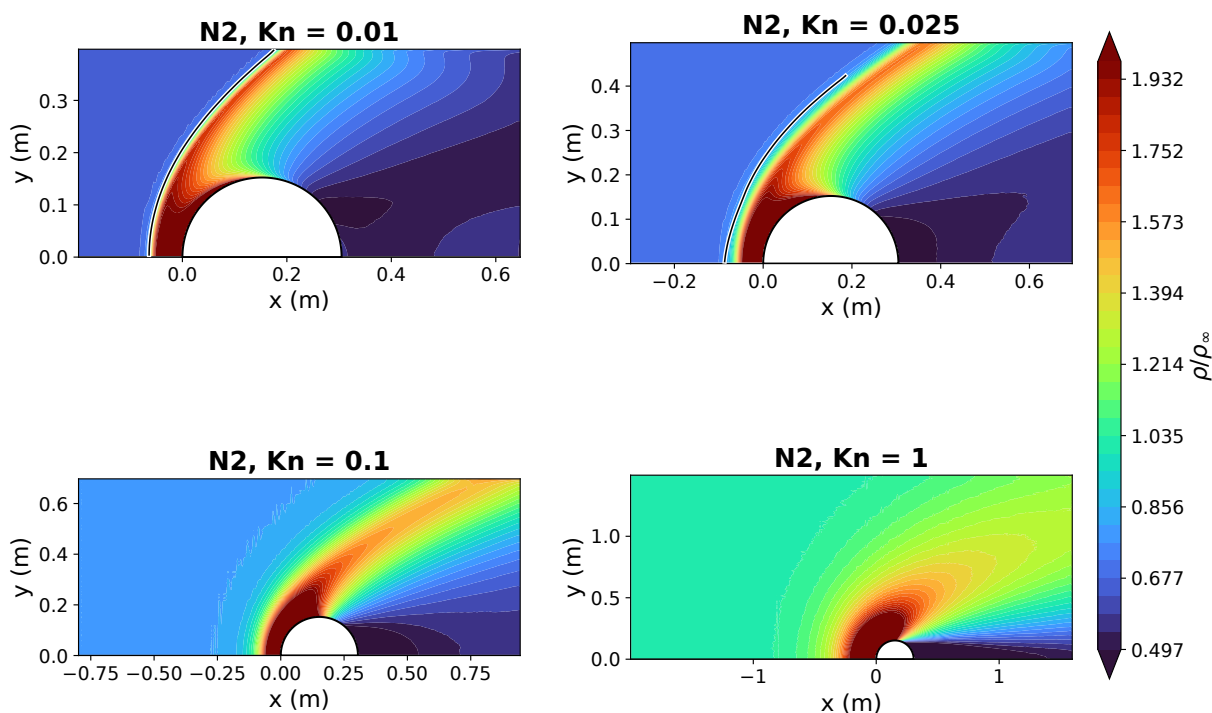
### 3.2 Mach-number variation at fixed rarefaction

Figure 3 shows the Mach-number dependence of the density field at fixed  $Kn_\infty = 0.01$ . At this low rarefaction level, the flow still retains a relatively continuum-like detached bow-shock structure. Increasing  $M_\infty$  strengthens the upstream compression and increases the normal-shock density jump. As a result, the gas can be decelerated and compressed over a shorter distance ahead of the cylinder, and the upstream branch of the bow shock moves closer to the body. Equivalently, the shock standoff distance decreases as the post-shock density and pressure rise become larger: a thinner compressed layer is sufficient to turn the flow around the blunt body. This trend is consistent with the classical continuum behaviour of detached shocks over blunt bodies, where the shock standoff distance decreases with increasing Mach number and approaches a high-Mach-number asymptote once the normal-shock compression ratio becomes nearly saturated.

The Mach-number sweep should therefore be interpreted differently from the Knudsen-number sweep. Varying  $M_\infty$  at fixed low  $Kn_\infty$  mainly changes the strength, curvature and standoff distance of an otherwise coherent bow shock. In contrast, increasing  $Kn_\infty$  changes the kinetic character of the layer itself: the mean free path becomes comparable to the shock-layer thickness, collisions are no longer frequent enough to maintain a narrow compression front, and the shock is replaced by a broad non-equilibrium compression layer. Thus, the Mach sweep produces a mostly geometric displacement and strengthening of the shock, whereas the Knudsen-number sweep produces a qualitative loss of a unique shock-front representation.



(a) Argon.



(b) Nitrogen.

Figure 2: Rarefaction-induced inflation of the hypersonic bow-shock layer over a circular cylinder at  $M_\infty = 10$ . The panels show the normalized density field  $\rho/\rho_\infty$  for increasing  $Kn_\infty$ . For the low- $Kn_\infty$  cases, where a distinct compression-front ridge exists, the detected front is overlaid. At larger  $Kn_\infty$ , the bow shock becomes a broad kinetic compression layer and no unique shock-line overlay is imposed. The colour scale is kept common within each gas to emphasize the growth of the compressed region. Since  $\rho/\rho_\infty = 1$  lies inside the colour range rather than at its lower bound, the undisturbed upstream state is not necessarily represented by the darkest blue colour. The upstream normalization was checked directly from the far-field DSMC samples for each case.

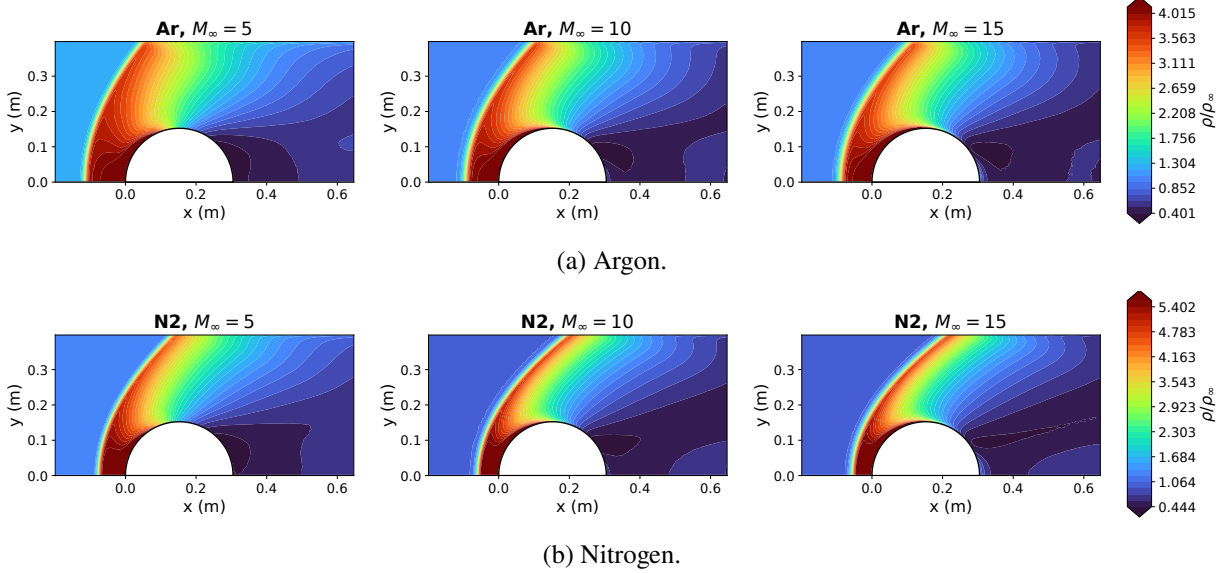


Figure 3: Mach-number dependence of the bow-shock structure at fixed  $Kn_\infty = 0.01$ . Increasing  $M_\infty$  strengthens the compression and moves the upstream bow-shock branch closer to the cylinder, consistent with the classical decrease of blunt-body shock standoff with Mach number. Unlike the Knudsen-number sweep, the shock layer remains comparatively sharp and coherent, showing that changing shock strength at low rarefaction does not produce the same kinetic delocalization as increasing  $Kn_\infty$ . Nitrogen exhibits a somewhat broader post-shock relaxation region because part of the shock-generated translational energy is redistributed into rotational modes.

The argon and nitrogen fields follow the same leading-order Mach trend, but their post-shock relaxation structures differ. In monatomic argon, the shock energy is accommodated only through translational degrees of freedom, so the density and translational-temperature adjustment remain more tightly coupled. In nitrogen, part of the shock-generated translational energy is transferred into rotational modes over a finite relaxation distance. This internal-energy exchange broadens the thermal relaxation region behind the density-compression front and makes the nitrogen shock layer less single-scale than the argon layer. Consequently, the gas dependence is not primarily a change in the existence of the bow shock at  $Kn_\infty = 0.01$ , but a change in how the post-shock non-equilibrium structure relaxes downstream of the compression front.

### 3.3 Quantitative shock-layer metrics

The density-contour visualizations establish the qualitative inflation of the bow-shock layer, but a quantitative comparison requires metrics that do not rely on manually drawing a single shock line in the high-Knudsen-number cases. We therefore extract the metrics directly from one-dimensional profiles sampled along body-normal rays. For each ray, the density-front location is defined as the position of the maximum radial density gradient. At low  $Kn_\infty$ , this location is interpreted as the shock-front position; at higher  $Kn_\infty$ , where no unique discontinuity exists, it is interpreted as the characteristic location of the strongest compression within the broad kinetic layer. The effective density thickness is computed as

$$\delta_\rho = \frac{|\rho_{\text{down}} - \rho_{\text{up}}|}{\max |\partial\rho/\partial r|}, \quad (9)$$

and is supplemented by a robust 10–90 thickness extracted from the normalized profile. These quantities are obtained from the local ray profiles and then summarized by the median over the upstream angular sector.

Thus the metrics used below do not require imposing a visible shock curve on the diffuse  $Kn_\infty = 0.1$  and 1 fields.

This distinction is essential for the high- $Kn_\infty$  cases. At  $Kn_\infty = 0.1$  and especially at  $Kn_\infty = 1$ , the maximum-gradient point is not treated as a discontinuity or as the unique physical shock location; it is only a reproducible marker of the strongest compression within a broad kinetic layer. The standoff and thickness metrics therefore describe the inflated compression layer, not a continuum shock surface.

Figure 4 quantifies the rarefaction-induced evolution of the density-compression layer. The key point is that this sweep is performed at fixed  $M_\infty = 10$ . In an inviscid hypersonic blunt-body picture, the leading-order standoff is organized primarily by the inverse normal-shock density ratio

$$\epsilon = \frac{\rho_\infty}{\rho_s} = \frac{\gamma - 1 + 2/M_\infty^2}{\gamma + 1}, \quad (10)$$

where  $\rho_s$  is the density immediately behind a normal shock. Hornung and co-workers showed that detached-shock standoff distances for spheres, cones, wedges and circular cylinders are strongly organized by this inverse post-shock density ratio, with extensions to non-equilibrium blunt-body flows through an effective density-ratio interpretation [Hornung, 1972, Hornung et al., 2019, Hornung, 2021]. In the present Knudsen-number sweep, however,  $\epsilon$  is approximately fixed for each gas. Therefore the systematic increase of the measured density-front standoff in figure 4(a) cannot be a normal-shock compression-ratio effect. It is a kinetic displacement: as the mean free path increases, the incoming directed kinetic energy is not converted into a localized post-shock compression over the same short collisional distance, and the strongest density-gradient response moves upstream.

A schematic way to express this distinction, used here as an interpretive decomposition rather than a fitted law, is

$$\frac{\Delta_s}{R} \simeq \Phi_{\text{inv}}(\epsilon) + \Phi_{\text{kin}}(Kn_s), \quad (11)$$

where  $R$  is the cylinder radius,  $\Phi_{\text{inv}}$  denotes the compression-ratio contribution, and  $Kn_s = \lambda_s/R$  is a representative post-shock or shock-layer Knudsen number. For the Mach sweep,  $\Phi_{\text{inv}}$  changes because  $\epsilon$  changes. For the Knudsen-number sweep,  $\Phi_{\text{inv}}$  is nearly fixed, while  $\Phi_{\text{kin}}$  grows with the mean free path. This explains why the Knudsen-number sweep inflates the compression layer even though the nominal shock strength is unchanged.

This interpretation is consistent with Hornung's analysis of non-equilibrium nitrogen flow over spheres and circular cylinders. There, finite-rate relaxation introduces a length scale behind the shock; as the relaxation rate decreases, the relaxation zone grows from a thin region near the shock into a layer occupying a substantial part of the shock layer. The present flow is non-dissociating, but the analogy is direct: increasing  $Kn_\infty$  reduces the collision rate responsible for local thermalization, so density and temperature adjust over a larger kinetic region. The high- $Kn_\infty$  panels should therefore be interpreted as finite-thickness kinetic compression layers, not as ordinary continuum shocks merely shifted away from the wall.

The thickness trend in figure 4(b) is governed by the same competition. Because  $\delta_\rho$  is defined by (9), it depends on both the density jump sampled across the compression layer and the peak density-gradient strength. Between  $Kn_\infty = 0.01$  and  $Kn_\infty \simeq 0.1$ , the compression front remains organized enough to maintain a strong gradient, while the effective density jump decreases as the post-shock state departs from the continuum-like normal-shock value. The ratio can therefore decrease, producing the observed shallow minimum in  $\delta_\rho$ . At larger  $Kn_\infty$ , the balance reverses: the peak gradient weakens, the compression is distributed over a larger kinetic distance, and the effective thickness becomes controlled by the local mean free path,

$$\delta_\rho/R = O(Kn_s), \quad Kn_s = \lambda_s/R. \quad (12)$$

Thus the increase of  $\delta_\rho$  at high  $Kn_\infty$  reflects breakdown of collisional localization rather than a change in inviscid shock compression.

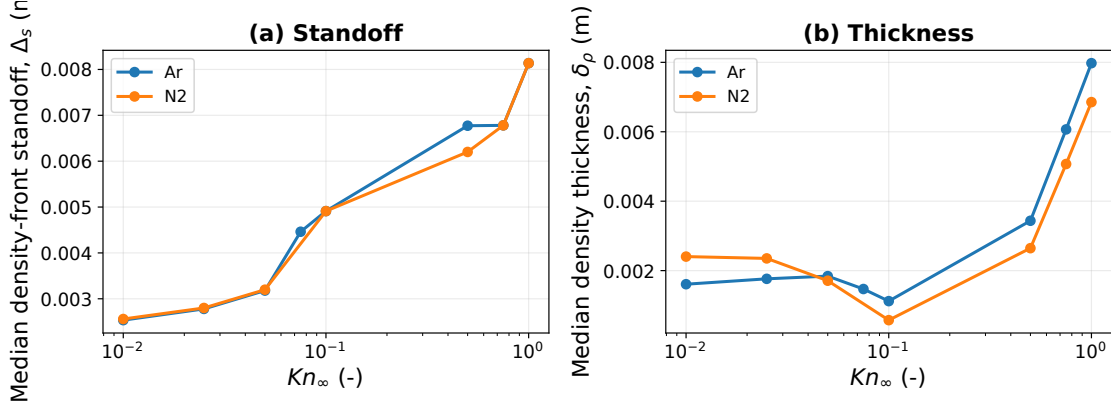


Figure 4: Density-based shock-layer metrics for the Knudsen-number sweep at  $M_\infty = 10$ . Panel (a) shows the median density-front standoff and panel (b) shows the effective density thickness  $\delta_\rho = |\rho_{\text{down}} - \rho_{\text{up}}| / \max |\partial\rho/\partial r|$ . Because  $M_\infty$  is fixed, the continuum normal-shock density ratio provides an approximately fixed low-rarefaction reference compression scale for each gas; the increase in standoff therefore reflects kinetic rarefaction rather than a change in inviscid shock-strength reference. The thickness has a shallow minimum near  $Kn_\infty \simeq 0.1$  because the sampled density jump and the peak density gradient vary in opposite ways. At higher  $Kn_\infty$ , collisional localization breaks down and the density change is distributed over a mean-free-path-controlled compression layer.

The argon and nitrogen curves follow the same leading-order trend, confirming that the density-layer inflation is primarily controlled by rarefaction. The remaining gas dependence is physically meaningful but secondary. In argon, all post-shock energy remains translational, so the density and translational temperature adjustments are tightly coupled. In nitrogen, rotational relaxation introduces an additional thermodynamic length scale behind the density front, modifying the detailed post-shock pressure and density adjustment without changing the dominant kinetic mechanism. Therefore figure 4 supports a Hornung-like interpretation in the low- $Kn_\infty$  limit, but shows that increasing  $Kn_\infty$  adds a mean-free-path-controlled inflation term absent from inviscid perfect-gas standoff correlations.

Figure 5 gives the corresponding density-based metrics for the Mach-number sweep at fixed  $Kn_\infty = 0.01$ . This sweep is the complementary limit to figure 4: the flow remains at low rarefaction, so the kinetic contribution to the standoff is comparatively small, but the inverse normal-shock density ratio  $\epsilon$ , defined in (10), changes with  $M_\infty$ . For a circular cylinder, the inviscid Hornung correlation can be written approximately as

$$\frac{\Delta}{R} \simeq 2.14 \epsilon \left(1 + \frac{\epsilon}{2}\right), \quad (13)$$

with the older near-linear form  $\Delta/R \simeq 2.32\epsilon$  giving a similar strong-shock trend [Hornung, 1972, 2021]. Although the present DSMC metric  $\Delta_s$  is the maximum-density-gradient location rather than the inviscid sonic-line standoff, the same compression-ratio scaling explains why increasing  $M_\infty$  moves the density-compression layer closer to the cylinder.

This scaling also explains the argon plateau in panel (a). For monatomic argon,  $\gamma = 5/3$ , and the normal-shock density ratio tends to the finite strong-shock limit  $(\gamma + 1)/(\gamma - 1) = 4$ , or  $\epsilon \rightarrow 0.25$ . The corresponding compression ratios at  $M_\infty = 5, 10$  and  $15$  are approximately 3.57, 3.88 and 3.95. Most of the available density compression has therefore already been achieved by  $M_\infty = 10$ . Increasing the Mach number from 10 to 15 still raises the kinetic energy and post-shock pressure, but it only weakly changes the density ratio controlling the leading geometric standoff; the argon curve therefore approaches a high-Mach asymptote.

The nitrogen standoff follows the same leading-order compression argument but need not coincide with

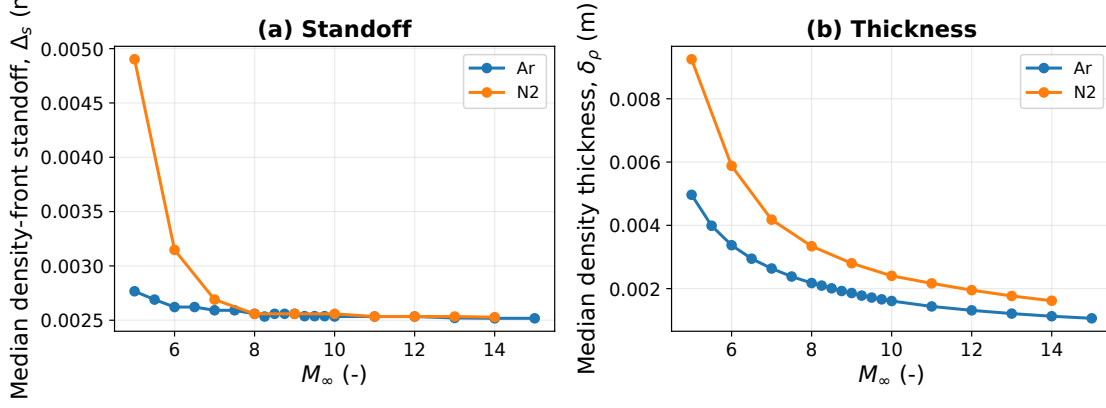


Figure 5: Density-based shock-layer metrics for the Mach-number sweep at fixed  $Kn_\infty = 0.01$ . Increasing  $M_\infty$  reduces the inverse normal-shock density ratio and moves the density-compression layer closer to the cylinder. The argon standoff approaches a high-Mach plateau because the normal-shock density ratio is already close to its strong-shock limit. The effective density thickness decreases because the peak density gradient strengthens faster than the sampled density jump grows. Nitrogen follows the same leading compression trend, with secondary differences associated with rotational relaxation behind the density front.

the argon curve. A calorically perfect diatomic estimate with  $\gamma \approx 1.4$  gives a strong-shock density-ratio limit of 6, which would favour a smaller inviscid standoff for the same body scale. In the DSMC nitrogen cases, however, finite rotational relaxation modifies the downstream pressure and temperature adjustment behind the density front. This is analogous to Hornung’s non-equilibrium nitrogen analysis, where density patterns over blunt bodies are sensitive to finite-rate relaxation; here the additional relaxation mechanism is rotational rather than chemical.

Panel (b) shows the corresponding effective density thickness, defined in (9). Its decrease with  $M_\infty$  is not simply a consequence of the density jump increasing. At fixed  $Kn_\infty = 0.01$ , the flow remains sufficiently collisional that stronger Mach-number compression is localized into a sharper density-gradient ridge. The density jump increases toward its strong-shock limit, but the peak gradient increases more rapidly than the jump itself, so the effective thickness decreases. This is opposite to the high- $Kn_\infty$  behaviour in figure 4, where rarefaction weakens the peak gradient and spreads the compression over a larger kinetic length.

Thus the four curves in figure 5 support a consistent interpretation: at fixed low  $Kn_\infty$ , increasing  $M_\infty$  primarily decreases  $\epsilon$ , moves the density-compression layer closer to the body and sharpens the density-gradient thickness. The behaviour is Hornung-like in the sense that the gross standoff is governed by post-shock compression, while the gas-dependent deviations reveal relaxation physics absent from a purely inviscid perfect-gas correlation. This is fundamentally different from the Knudsen-number sweep, where the loss of collisional localization, rather than the normal-shock compression ratio, controls the growth of the shock-layer thickness.

The same trends are summarized in Appendix B.1 using empirical diagnostic fits of the extracted standoff and thickness metrics. Those fits are not introduced as universal shock correlations; they are used only as compact summaries of the DSMC-derived trends. In particular, the Knudsen-sweep standoff fit highlights the monotonic kinetic displacement of the strongest compression marker, whereas the density-thickness fit emphasizes the shallow intermediate-  $Kn_\infty$  minimum followed by high-  $Kn_\infty$  broadening.

The same ray-based extraction can be applied to variables other than density. Figure 6 shows the resulting variable-specific scales for the argon Knudsen-number sweep. This diagnostic is deliberately shown for the monatomic gas, because argon has no rotational relaxation mode: any scale separation observed here is therefore not caused by internal-energy nonequilibrium, but by the different ways in which

density, momentum, pressure and translational energy respond across a finite kinetic shock layer.

Panel (a) shows that the absolute thicknesses do not grow at the same rate. The density thickness remains the smallest scale over most of the sweep, because it is tied to the strongest density-gradient ridge. By contrast, the Mach-number thickness becomes much larger. This is expected because the Mach number depends on both the flow speed and the local speed of sound, and hence on the coupled velocity and translational-temperature relaxation. The velocity deceleration and thermal adjustment extend over a broader region than the density-gradient maximum, especially once the mean free path is no longer small compared with the shock-layer thickness. The pressure and translational temperature scales occupy an intermediate range. Pressure is not simply a copy of density: in a rarefied shock layer,  $p \sim \rho T_{tr}$ , so density compression and translational heating can partially compensate or reinforce each other along different parts of the layer.

Panel (b) makes this scale separation more explicit by normalizing each variable thickness by  $\delta_\rho$ . The large values of  $\delta_M/\delta_\rho$  and  $\delta_p/\delta_\rho$ , particularly in the intermediate- $Kn_\infty$  regime, show that density is a poor universal reference length for the full macroscopic adjustment. Around  $Kn_\infty \approx 0.1$ , the density-gradient layer is still relatively sharp, whereas the velocity and pressure adjustments have already spread over a much larger kinetic region. This produces the large peak in the scale ratios. At higher  $Kn_\infty$ , the ratios decrease not because the fields recover a single-scale structure, but because the density reference scale itself becomes large and diffuse as collisional localization breaks down. Thus the apparent reduction of  $\delta_q/\delta_\rho$  at the largest  $Kn_\infty$  should be interpreted as the broadening of the density layer, not as restoration of continuum-like similarity.

Panel (c) compares the gradient-based thickness with the robust 10–90 transition thickness. The large values of  $\delta_{10-90}/\delta_\nabla$  for density indicate that the density profile contains a sharp local ridge embedded in a much broader finite-thickness transition. In other words, the maximum gradient identifies the most intense part of the compression layer, but it does not represent the full spatial extent of the density adjustment. The pressure and temperature ratios are much smaller because these fields vary more smoothly and are less dominated by a single narrow ridge. This distinction is important for the interpretation of high- $Kn_\infty$  shock metrics: the density-front location and  $\delta_\rho$  are useful local diagnostics, but they should not be mistaken for a complete shock-layer thickness when the profile has long kinetic tails.

Overall, figure 6 shows that rarefaction creates a hierarchy of macroscopic length scales even in monatomic argon. The density compression, velocity/Mach deceleration, pressure adjustment and translational heating do not share one universal thickness. This supports the central interpretation of the paper: the inflated bow shock is not simply a translated and rescaled continuum shock, but a finite kinetic layer in which different moments of the distribution function relax over different distances.

For completeness, figure 7 reports the variable-specific scales in the Mach-number sweep at fixed  $Kn_\infty = 0.01$ . This figure should be interpreted together with figure 5. At this low rarefaction level, the density-compression layer remains localized, but increasing  $M_\infty$  changes how different macroscopic variables adjust across the shock. The density thickness decreases with Mach number because the stronger shock produces a sharper density-gradient ridge. This decrease of  $\delta_\rho$  is the reference against which the other scales are normalized.

The important feature is that the other variables do not decrease in the same way. The Mach-number thickness increases relative to the density thickness, especially in nitrogen, because the Mach number depends simultaneously on flow deceleration and translational heating through the local sound speed. These two processes need not occur over the same distance as the density jump. Pressure also develops a larger relative scale than density, since  $p \sim \rho T_{tr}$  and therefore combines density compression with translational thermal relaxation. The translational-temperature scale is smoother and varies more weakly, while the nitrogen rotational-temperature scale remains distinct, reflecting the finite distance required for rotational energy exchange behind the density front.

Panel (b) therefore does not imply that the Mach sweep destroys the shock structure in the same way as the Knudsen-number sweep. Rather, because  $\delta_\rho$  becomes smaller as the shock strengthens, even moderate absolute differences between the density, pressure, Mach-number and thermal thicknesses become amplified

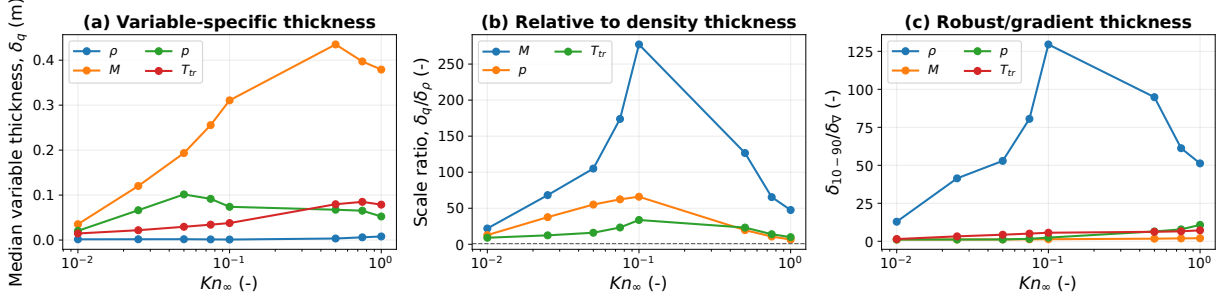


Figure 6: Variable-specific shock-layer scales for argon in the Knudsen-number sweep. Panel (a) shows the absolute gradient-based thicknesses for density, Mach number, pressure and translational temperature. Panel (b) normalizes the same scales by the density thickness,  $\delta_q/\delta_\rho$ , and demonstrates that density is not a universal reference scale for the full macroscopic adjustment. Panel (c) compares the robust 10–90 transition thickness with the local gradient thickness. The large density ratio indicates that a sharp density-gradient ridge is embedded within a broader finite kinetic transition, whereas pressure and temperature vary more smoothly. The result shows that multi-scale shock-layer structure appears even in monatomic argon, before any rotational or internal-energy relaxation is introduced.

when expressed as  $\delta_q/\delta_\rho$ . This is why the scale ratios increase with  $M_\infty$ , although the contour plots and the profile-collapse results still show a coherent attached shock layer.

Panel (c) further separates local-gradient thickness from full transition width. For both gases, the density  $\delta_{10-90}/\delta_\nabla$  ratio increases with  $M_\infty$ , showing that the density profile contains a very sharp maximum-gradient region embedded within a broader finite transition. The thermal and pressure ratios remain much closer to unity, indicating smoother monotonic adjustments without the same degree of local ridge sharpening. Thus the Mach sweep preserves a compact shock layer, but it also reveals that the density-gradient scale becomes progressively more localized than the velocity, pressure and thermal relaxation scales. This behaviour is consistent with the Hornung-type interpretation of Mach variation as primarily a change in compression ratio and shock strength, rather than a mean-free-path-driven delocalization of the entire compression layer.

### 3.4 Shock-attached similarity and its breakdown

The preceding metrics show that the density-gradient location and thickness provide useful local measures of the compression layer, but they do not by themselves establish whether the entire shock layer is governed by one similarity scale. We therefore test the stronger hypothesis that the shock sector can be collapsed by using the density-compression centre and the density-gradient thickness as the common registration variables. Each field is sampled along body-normal rays in the upstream shock sector, and the profiles are registered using

$$\xi_\rho = \frac{s - s_\rho}{\delta_\rho}, \quad (14)$$

where  $s$  is the distance along the body-normal ray,  $s_\rho$  is the maximum-density-gradient location, and  $\delta_\rho$  is the local density-gradient thickness. Each variable is then normalized by its own local upstream and downstream values across the same density-defined layer. This construction deliberately uses the density field to align all variables. It therefore asks whether velocity, pressure and thermal relaxation are slaved to the density-compression scale, or whether they retain additional length scales after the density layer has been aligned. The purpose is not to find the optimal coordinate for each variable separately, but to test whether the density-compression layer provides a universal organizing coordinate for the full shock layer. For the highest- $Kn_\infty$  cases, this coordinate should be understood as a compression-layer coordinate based on the

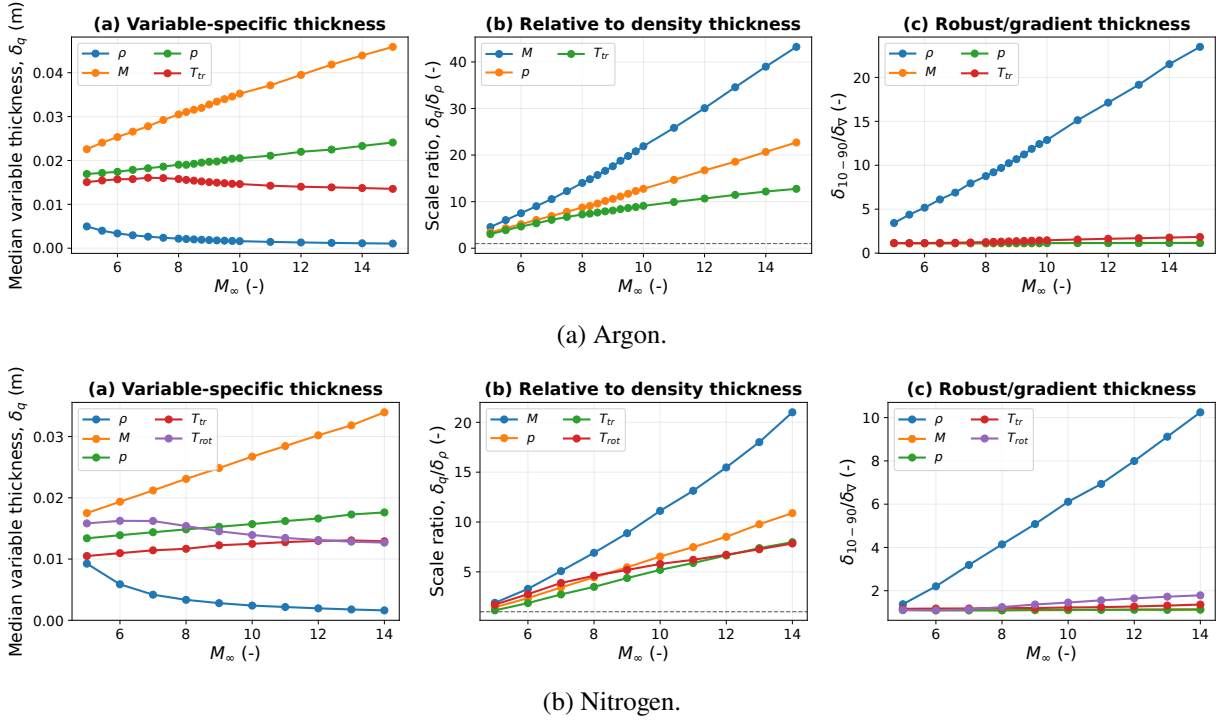


Figure 7: Variable-specific shock-layer scales in the Mach-number sweep at  $Kn_\infty = 0.01$ . Panel (a) shows the absolute gradient-based thicknesses of density, Mach number, pressure, translational temperature and, for nitrogen, rotational temperature. Panel (b) normalizes these scales by the density thickness. The increase of  $\delta_q/\delta_\rho$  with  $M_\infty$  occurs because the density-gradient layer sharpens as the shock strengthens, whereas velocity, pressure and thermal relaxation remain distributed over broader distances. Panel (c) compares the robust 10–90 transition width with the local gradient thickness. The growing density ratio indicates that a narrow maximum-gradient ridge is embedded within a broader density transition, while pressure and temperature vary more smoothly. Thus the Mach sweep preserves a coherent attached shock layer, but the density scale becomes increasingly localized relative to the other macroscopic adjustment scales.

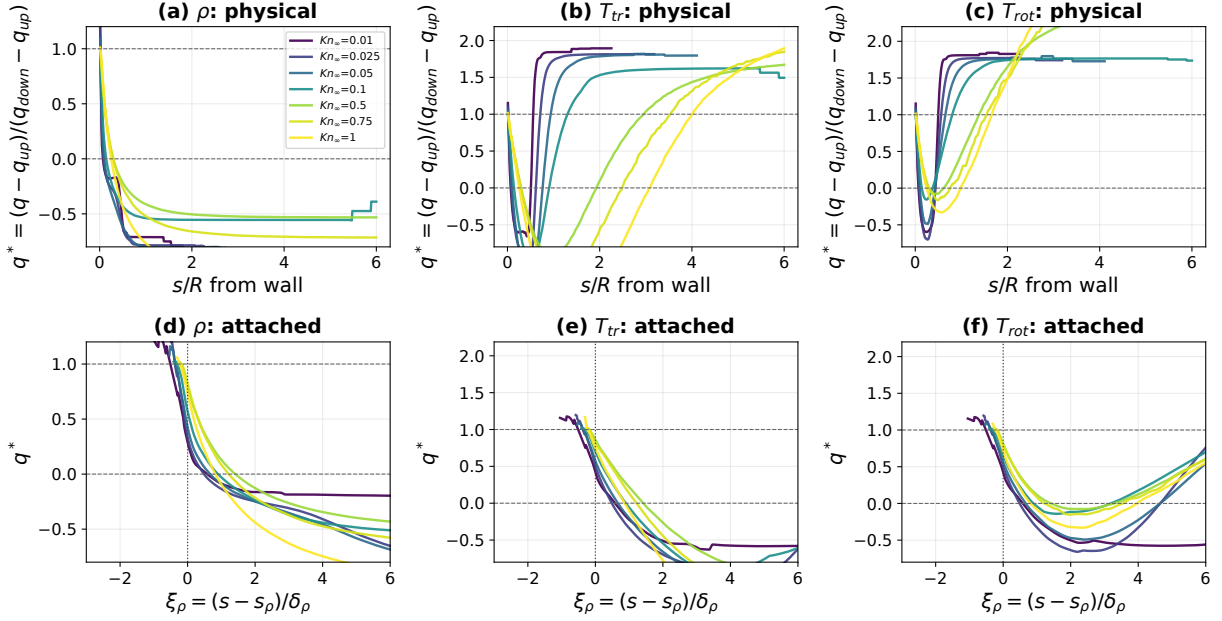


Figure 8: Physical and density-registered shock-sector profiles for nitrogen in the Knudsen-number sweep at  $M_\infty = 10$ . The profiles are median profiles sampled over body-normal rays in the upstream shock sector. The top row shows normalized profiles in the physical coordinate  $s/R$ , while the bottom row shows the same profiles in the density-attached coordinate  $\xi_\rho = (s - s_\rho)/\delta_\rho$ . The density field becomes much more compact after registration, showing that the geometric inflation of the compression layer is largely captured by  $s_\rho$  and  $\delta_\rho$ . The translational and rotational temperature profiles retain residual downstream spread, demonstrating that thermal/internal relaxation is not governed by a single density-compression scale.

strongest density-gradient marker, not as a coordinate attached to a discontinuous shock surface.

Figure 8 shows this test for the nitrogen Knudsen-number sweep. Nitrogen is the most demanding case because, in addition to density compression and translational heating, rotational relaxation provides a separate internal-energy adjustment process. In physical coordinates, the profiles move and broaden as  $Kn_\infty$  increases, consistent with the standoff and thickness trends in figure 4. After density-based registration, the main density-transition region is more closely aligned in the attached coordinate, indicating that a substantial part of the geometric displacement of the compression layer is represented by  $s_\rho$  and  $\delta_\rho$ . The collapse is not complete: the registered density profiles still retain downstream tail differences, especially at larger  $Kn_\infty$ . The thermal fields show a similar alignment of the leading transition near  $\xi_\rho = 0$ , but their downstream relaxation portions remain more strongly parameter-dependent. Thus the profile registration removes the dominant geometric shift, while the residual spread of  $T_{tr}$  and  $T_{rot}$  indicates additional thermal/internal relaxation scales beyond the density-compression coordinate.

The failure of the thermal profiles to collapse completely is consistent with the variable-scale analysis in figures 6 and 7. Density marks the most intense compression ridge, but thermal and internal-energy variables respond to both compression and post-shock relaxation. As  $Kn_\infty$  increases, the collision length becomes comparable to the shock-layer scale, so equilibration no longer occurs within a narrow density-gradient layer. The registered profiles therefore show the same physics as the thickness metrics: the high- $Kn_\infty$  bow shock is not simply a displaced and broadened version of a low- $Kn_\infty$  shock, but a finite kinetic compression-relaxation layer with multiple macroscopic scales.

The corresponding Mach-number sweep is shown in figure 9. This case provides the complementary

limit to figure 8. Here  $Kn_\infty = 0.01$  is fixed, so the mean free path remains small relative to the body scale and the shock layer remains comparatively localized. Increasing  $M_\infty$  changes the compression ratio, shock curvature and standoff distance, as discussed in figures 3 and 5, but it does not introduce the same mean-free-path-driven delocalization seen in the Knudsen-number sweep. Consequently, density-based registration produces a more coherent family of density profiles than in the Knudsen-number sweep.

The thermal profiles in figure 9, especially  $T_{tr}$  for the lowest Mach numbers, should be interpreted with this normalization in mind. At  $M_\infty = 5\text{--}6$  the shock is weaker, the translational-temperature jump across the density-defined layer is smaller, and the imposed diffuse-wall temperature is comparatively more influential relative to the shock-heated gas than it is at larger Mach numbers. In nitrogen, part of the translational energy is also transferred into rotation over a finite distance behind the density front. The normalized quantity  $q^* = (q - q_{up}) / (q_{down} - q_{up})$  therefore amplifies the low-Mach translational-temperature response: small differences in the downstream thermal plateau and in the wall-adjacent portion of the ray appear as a larger departure in the normalized  $T_{tr}$  profiles. This behaviour is not used here as a separate low-Mach thermal-similarity regime; it indicates that thermal normalization and relaxation are more sensitive than density compression when the shock heating is weak.

The residual differences in figure 9 should therefore be interpreted differently from those in figure 8. In the Mach sweep, the spread mainly reflects changes in shock strength, thermal jump amplitude and post-shock thermodynamic level at fixed low rarefaction. The density front remains a meaningful organizing structure, and the profile family is closer to a single attached-layer description than in the Knudsen-number sweep. In the Knudsen-number sweep, by contrast, the spread reflects the emergence of a kinetic relaxation length that is not captured by density registration alone. The comparison of figures 8 and 9 therefore separates two mechanisms: Mach-number variation changes the strength of a coherent shock and the relative thermal jump scale, whereas Knudsen-number variation changes the kinetic nature of the shock layer itself.

### 3.5 Compact multi-modal structure

The profile-collapse results show that density registration removes much of the geometric displacement and broadening of the shock layer, but they also show that non-density variables retain residual structure. We therefore use proper orthogonal decomposition (POD) as a parameter-space compactness diagnostic. The snapshots are indexed by  $Kn_\infty$  or  $M_\infty$ , rather than by time, so the POD modes are not interpreted as temporal instability modes. Following the standard data-based interpretation of POD, the singular values identify how many coherent spatial directions are required to represent the registered family of DSMC fields. In the present usage, “nearly rank one” means that the leading mode captures almost all of the fluctuation variance. For the maximum-density-gradient registered density fields considered here, this corresponds to  $E_1 = 0.974$  for argon and  $E_1 = 0.986$  for nitrogen in the Knudsen-number sweep (table 2), i.e. 97.4–98.6% of the variance. Slower modal decay indicates that additional coherent structures remain after registration. The interpretation is physical only at the level of the organized leading patterns: density modes primarily describe residual compression-layer displacement and broadening; Mach-number modes include the combined effects of velocity deceleration, sound-speed variation and shock curvature; translational-temperature modes reflect shock heating and finite wall-temperature interaction; and rotational-temperature modes in nitrogen measure the additional internal-energy relaxation scale. Higher-order modes are not interpreted individually because they can contain contributions from DSMC sampling scatter, finite snapshot number and details of the common-support mask.

The two-dimensional POD is constructed as follows. For each variable and each case, the registered field  $q^*(\theta, \xi_q)$  is sampled on the common  $65 \times 260$   $(\theta, \xi_q)$  grid described above. Points that are outside the common valid support for more than 30% of the snapshots are excluded from the inner product, which prevents extrapolated white regions from influencing the modes. Each remaining two-dimensional field is flattened into a row vector, the snapshot mean is subtracted, and singular-value decomposition (SVD) is

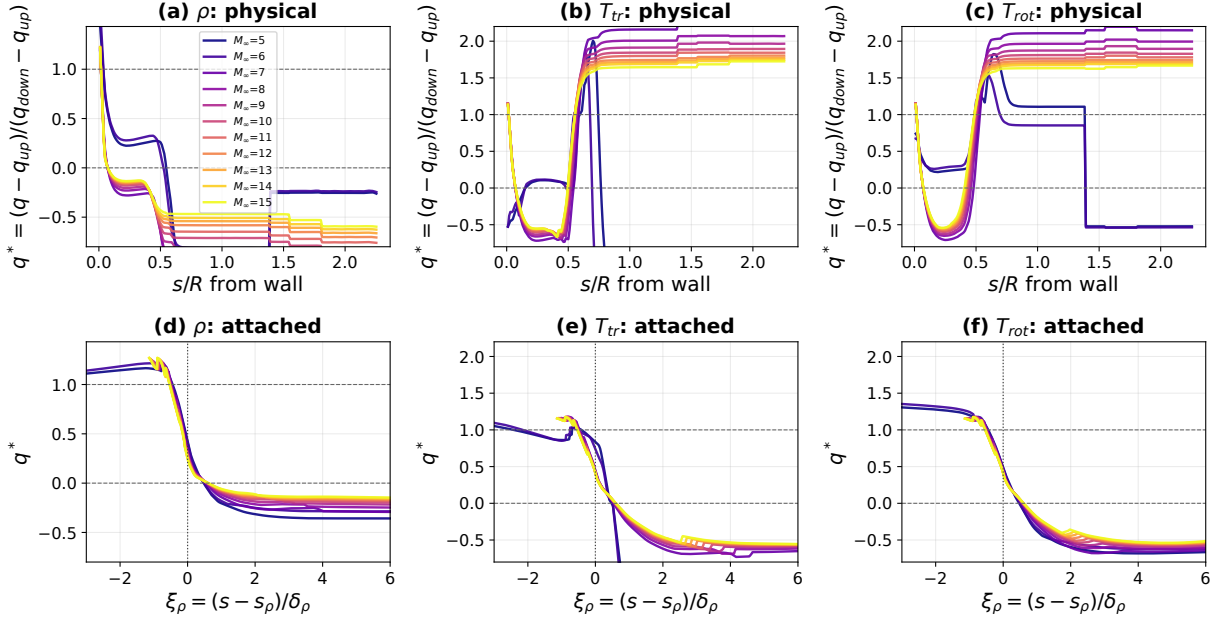


Figure 9: Physical and density-registered shock-sector profiles for nitrogen in the Mach-number sweep at fixed  $Kn_\infty = 0.01$ . The top row shows normalized profiles in the physical coordinate  $s/R$ , and the bottom row shows the same profiles in the density-attached coordinate  $\xi_\rho = (s - s_\rho)/\delta_\rho$ . Compared with the Knudsen-number sweep, density-based registration gives a more coherent alignment of the density transition, indicating that changing  $M_\infty$  at low rarefaction primarily changes shock strength, curvature and thermodynamic level rather than producing broad kinetic delocalization. The low-Mach translational temperature profiles are more distinct because the translational-temperature jump is weaker and the wall-adjacent/post-shock thermal levels have greater relative influence in the normalized variable  $q^*$ . The thermal panels are therefore interpreted as diagnostic evidence of finite relaxation and normalization sensitivity, not as evidence of a separate numerical failure or of a universal thermal collapse. The low-Mach  $T_{tr}$  curves are more sensitive to the local upstream/downstream normalization because the thermal jump is weaker and the thermal-transition location differs more strongly from the high-Mach cases. Dimensional  $T_{tr}$  profiles remain monotonic with  $M_\infty$ ; the normalized low-Mach behaviour is therefore interpreted as a diagnostic normalization sensitivity of the weak-shock thermal layer.

applied to the matrix  $\mathbf{X} \in \mathbb{R}^{N_s \times N_p}$ , where  $N_s$  is the number of snapshots and  $N_p$  is the number of retained valid grid points. No additional quadrature weighting is applied; because the attached grid is uniform in  $\theta$  and  $\xi_q$ , the discrete Euclidean inner product is equivalent to a constant-weight approximation of the attached-coordinate energy. The modal energy is  $E_i = \sigma_i^2 / \sum_j \sigma_j^2$ , and the cumulative energy is  $C_i = \sum_{j=1}^i E_j$ , where  $\sigma_i$  is the  $i$ th singular value. These modal energies are variance fractions in the chosen attached-coordinate representation; they are not physical kinetic, thermal or thermodynamic energy norms. A geometry- or Jacobian-weighted inner product would define a different norm, whereas the present constant-weight norm is used consistently for all variables so that modal compactness can be compared within the same registration framework.

The normalization  $q^* = (q - q_{\text{up}}) / (q_{\text{down}} - q_{\text{up}})$  removes the leading jump amplitude and emphasizes the registered transition shape. The resulting POD energies should therefore be read as compactness measures of normalized shock-layer structure rather than as amplitudes of dimensional fluctuations.

The number of parameter snapshots is necessarily limited by the DSMC data set: the Knudsen-number sweep contains eight snapshots, while the Mach-number sweep contains eleven snapshots. After common-support masking, the number of retained spatial grid points changes between variables, but the number of snapshots in each sweep is fixed. Consequently, the maximum possible number of non-zero POD modes is small, and low rank can partly arise from the finite size of the parameter sweep. We therefore do not interpret the higher modes as a complete statistical basis, and the 95% mode count in the tables is only a compactness diagnostic rather than validation of a predictive reduced-order model. Instead, the POD is used comparatively: density, pressure, Mach number and thermal variables are processed with the same grid, masks, normalization and SVD procedure. Differences in modal decay therefore indicate differences in attached-layer compactness within the same finite data set.

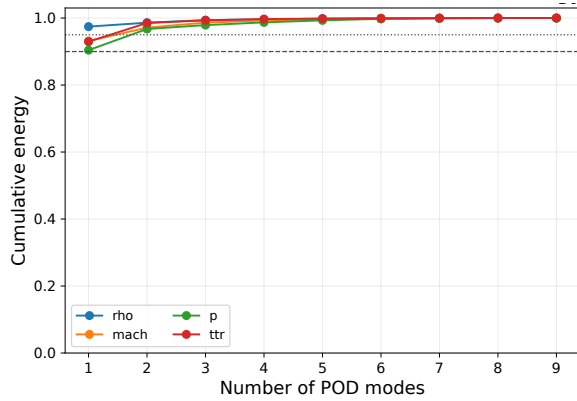
Appendix B.2 and Appendix B.3 report leave-one-out checks in which each Knudsen-number snapshot is omitted in turn. These checks are not substitutes for a larger parameter ensemble, but they test whether the compactness ordering is controlled by one individual snapshot and whether the retained modes can reconstruct an excluded parameter state. The results support the central interpretation within the available data: the density mode is stable to snapshot removal, whereas Mach number and the thermal variables retain larger leave-one-out variation and therefore should not be interpreted as single-mode registered families.

Appendix B.4 also reports two additional checks aimed at the modal interpretation itself. First, the POD coefficients are plotted as functions of  $Kn_\infty$ , so that the leading modes are connected to coherent parameter-dependent amplitudes rather than only to singular values. Second, the POD is repeated with moderate coordinate-space weights and with restricted attached-coordinate windows. These tests do not change the compactness ordering:  $\rho$  remains the most compact registered field,  $p$  is intermediate, and  $M$ ,  $T_{rr}$  and  $T_{rot}$  retain additional modal content.

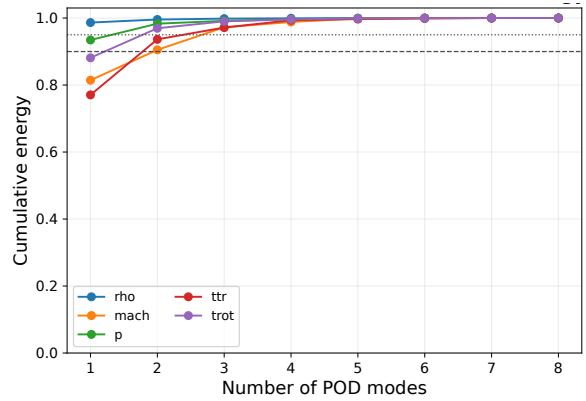
Representative block-based intervals for the extracted standoff and thickness metrics are listed in Appendix B.5, and additional Mach-sweep modal diagnostics are collected in Appendix C.

Figure 10 shows the cumulative POD energy for the two-dimensional shock-attached fields in the Knudsen-number sweep. Within the present maximum-density-gradient shock-attached registration, the density field is nearly rank one in this quantitative sense: the leading mode captures 97.4% of the argon density variance and 98.6% of the nitrogen density variance (table 2). This confirms that the density compression layer admits a compact attached representation. The thermal fields are less compact. In nitrogen, the leading modes of  $T_{rr}$  and  $T_{rot}$  capture 88.7% and 86.2%, respectively, and the second modes raise the corresponding cumulative energies to 94.1% and 96.5%. The first two rotational-temperature modes already exceed the 95% threshold, but the need for a second organized mode still shows that the residual thermal variation is not captured by a single registered template. Hence the loss of complete similarity is not caused only by shock displacement or thickness variation; thermal and internal relaxation retain their own modal content.

Before examining the spatial POD modes, we quantify how much density-attached registration changes



(a) Argon.



(b) Nitrogen.

Figure 10: Cumulative POD energy of shock-attached fields in the Knudsen-number sweep at  $M_\infty = 10$ . The density leading mode captures 97.4–98.6% of the registered density variance, while the nitrogen translational and rotational temperature fields require additional modes. The spectra are used comparatively across variables processed with the same grid, masks and normalization, rather than as absolute universal modal energies. They quantify the contrast already visible in the density-registered profiles: density admits a compact attached-layer description, but thermal/internal-energy relaxation retains residual multi-scale structure.

Table 2: POD compactness of shock-attached fields in the Knudsen-number sweep. Here  $E_1$  is the leading fractional POD energy and  $C_2 = E_1 + E_2$  is the cumulative energy captured by the first two modes.

Gas	Variable	$E_1$	$C_2$	Modes for 95%
Ar	$\rho$	0.974	0.986	1
Ar	$T_{tr}$	0.930	0.985	2
N2	$\rho$	0.986	0.996	1
N2	$M$	0.578	0.812	4
N2	$p$	0.803	0.970	2
N2	$T_{tr}$	0.887	0.941	3
N2	$T_{rot}$	0.862	0.965	2

Table 3: Effect of density-attached registration on the POD compactness of nitrogen shock-sector profiles in the Knudsen-number sweep. The columns compare the leading POD energy in the physical coordinate and in the density-attached coordinate;  $C_2$  is reported for the density-attached profiles.

Variable	$E_1$ , physical	$E_1$ , density-attached	$C_2$ , density-attached
$\rho$	0.924	0.998	0.999
$M$	0.911	0.775	0.925
$p$	0.763	0.940	0.991
$T_{tr}$	0.885	0.853	0.981
$T_{rot}$	0.766	0.921	0.992

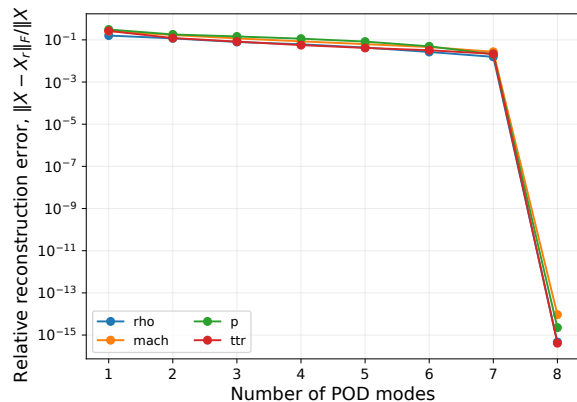
the compactness of the one-dimensional shock-sector profile families. These profile POD values are not intended to be numerically identical to the two-dimensional field POD values in table 2, because the data matrices and normalization domains are different. Table 3 compares the leading POD energy  $E_1$  for nitrogen profiles in the physical coordinate and in the density-attached coordinate. A table is used rather than a bar chart because the important information is the selective change in modal compactness for each variable, not the graphical height of bars. The density profiles become almost rank one after registration, confirming that the geometric displacement and broadening of the density-compression layer are largely removed by  $s_\rho$  and  $\delta_\rho$ . Pressure and rotational temperature also gain compactness, indicating that part of their variation follows the density-layer motion. By contrast, Mach number and translational temperature do not gain the same leading-mode compactness. This is consistent with the scale analysis above: Mach number combines velocity deceleration and local sound-speed variation, while  $T_{tr}$  reflects translational energy relaxation downstream of the density ridge. These variables therefore retain structure that is not removed by density-based registration alone.

These profile POD values are not directly comparable to the two-dimensional field POD values in table 2, because the data matrices and normalization domains are different. The table is included to quantify how registration changes one-dimensional shock-sector profiles; the two-dimensional field compactness, including the nitrogen Mach-number and pressure fields shown in the spectra, is summarized separately in table 2 and Appendix A.

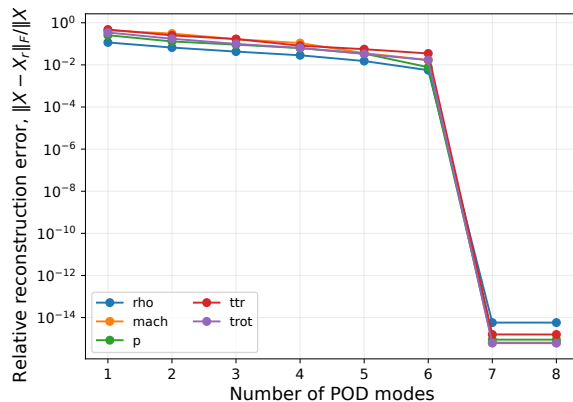
The decrease of the Mach-number leading energy after density-attached registration, from 0.911 in physical coordinates to 0.775 in attached coordinates, is a useful counter-example to a purely geometric interpretation of the registration. Density registration removes the dominant displacement and broadening of the density-compression layer, but the Mach number is a composite quantity involving both velocity deceleration and the local speed of sound. Once the density motion is removed, the remaining Mach-number variability is not well represented by a single attached template and is redistributed into the second mode, as reflected by  $C_2 = 0.925$ . This behaviour supports the conclusion that Mach-number similarity is not completely slaved to the density front: density alignment removes the dominant geometric motion, but it does not simultaneously align the velocity deceleration and sound-speed variation that define the Mach field.

Figure 11 shows the corresponding reconstruction error for the two-dimensional fields. The density error decreases rapidly with the first mode, whereas the nitrogen thermal fields require additional modes to reach the same accuracy. This reinforces the conclusion that shock-attached density collapse does not imply full thermodynamic similarity.

The registration-gain table and reconstruction-error curves show that the non-density variables retain additional structure after alignment. The spatial organization of this residual thermal content is shown in figure 12. We show only the mean and the first two thermal POD modes because the spectra and the compactness measures already establish that the remaining variability is low-dimensional. The important



(a) Argon.



(b) Nitrogen.

Figure 11: Relative POD reconstruction error for shock-attached fields in the Knudsen-number sweep. The error curves complement the cumulative-energy spectra and show that nitrogen thermal fields retain residual structure beyond the leading mode.

point is not merely that more than one mode is present, but that the additional modes are organized within the finite compression–relaxation layer.

The modelling implication is that a reduced-order or neural-operator representation of rarefied hypersonic bow shocks should not rely only on a single density-attached coordinate. Such a coordinate is highly effective for compressing the density field and for removing much of the apparent geometric inflation, but additional state variables or latent coordinates are needed to represent velocity, pressure and thermal relaxation with comparable accuracy. For nitrogen, in particular, the translational and rotational temperatures retain coherent downstream and angular structures after density registration; these structures are precisely the components that a single-scale shock-shift model would miss.

## 4 Conclusions

This study examined whether rarefied hypersonic bow-shock inflation over a circular cylinder is a simple displacement and broadening of one shock layer, or whether different moments of the gas distribution retain distinct attached-layer scales. DSMC data for argon and nitrogen were analysed over a Knudsen-number sweep at  $M_\infty = 10$  and a Mach-number sweep at  $Kn_\infty = 0.01$ . At low rarefaction, the ray-based density-gradient ridge agrees with an independent SWD shock-centre extraction, confirming that a reproducible shock-front location exists when the shock remains sufficiently narrow. At higher  $Kn_\infty$ , the same diagnostic no longer represents a unique discontinuity; it identifies the strongest compression location inside a broad kinetic layer.

The density-based metrics separate the two mechanisms. In the Mach sweep,  $Kn_\infty$  is fixed and increasing  $M_\infty$  mainly changes the inverse normal-shock density ratio, shock strength and curvature. The density front moves closer to the cylinder and the density-gradient layer sharpens while the shock remains comparatively coherent. In the Knudsen-number sweep,  $M_\infty$  is fixed, so the inviscid compression parameter is nearly fixed; the increase in standoff and the high- $Kn_\infty$  growth of thickness are therefore kinetic effects associated with the loss of collisional localization. The intermediate minimum in the effective density thickness reflects the competition between a decreasing sampled density jump and a weakening maximum density gradient.

The variable-scale, profile-collapse and POD analyses show that, within the present two-dimensional cylinder benchmark, gas models and parameter ranges, the inflated layer is not governed by one universal

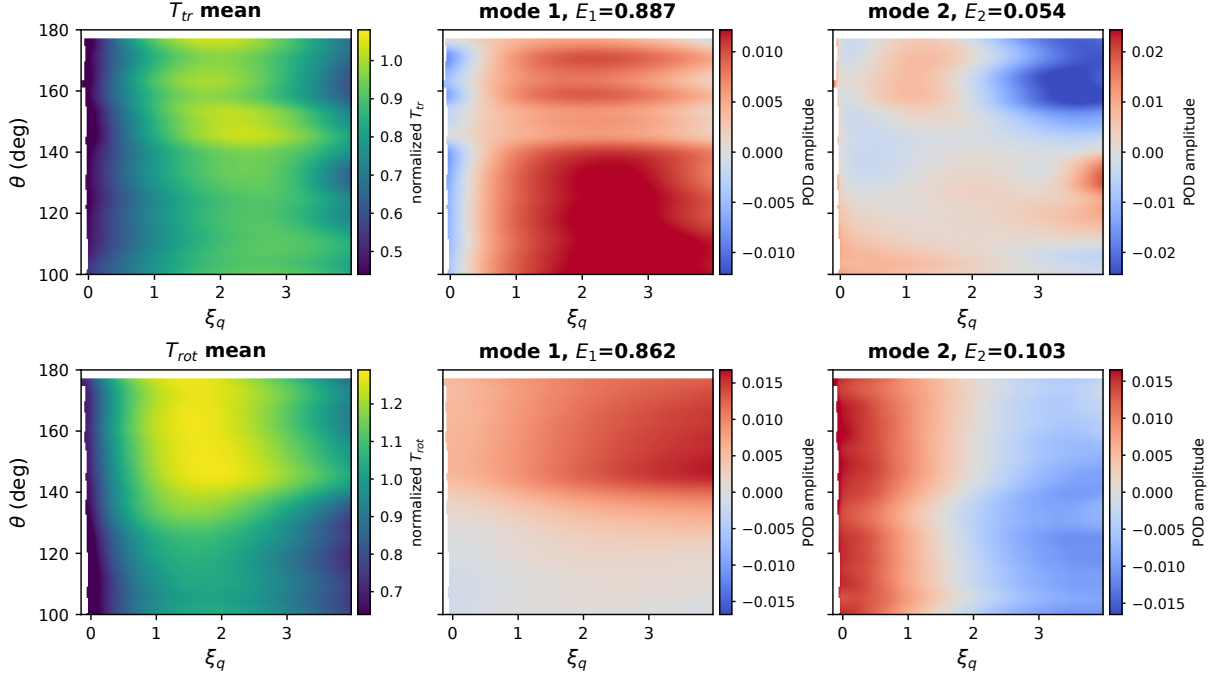


Figure 12: Shock-attached POD modes of the nitrogen thermal fields in the Knudsen-number sweep. The upper row shows the mean, first mode and second mode of the translational-temperature field  $T_{tr}$ , while the lower row shows the corresponding rotational-temperature structures  $T_{rot}$ . The mode energies are written on the panels: for  $T_{tr}$ ,  $E_1 = 0.887$  and  $E_2 = 0.054$ ; for  $T_{rot}$ ,  $E_1 = 0.862$  and  $E_2 = 0.103$ . White regions denote points outside the common valid support of the shock-attached interpolation and are not included in the POD inner product. The mean-field colour bars show the normalized temperatures, whereas the modal colour bars show signed POD amplitudes with symmetric limits. The maps are displayed with mild masked smoothing for visualization only; the POD modes and modal energies are computed from the unsmoothed registered fields. Because POD modes are defined up to an arbitrary sign, the interpretation is based on the spatial organization of the patterns rather than on the absolute sign of the plotted amplitudes. The modes are spatially organized within the finite compression–relaxation layer: the leading mode represents the dominant registered relaxation pattern, while the second mode captures secondary angular redistribution and downstream-tail variation across  $\theta$  and  $\xi_q$ . The spatial organization of the leading modes is consistent with coherent thermal-relaxation structure beyond local DSMC sampling scatter.

thickness. Under the maximum-density-gradient registration used here, the density field becomes almost rank one, but the profile-level registration test shows that this compactness is selective: pressure and rotational temperature partly follow the density-layer motion, whereas Mach number and translational temperature retain independent modal content. The nitrogen thermal POD modes are spatially organized within the compression–relaxation layer and are consistent with coherent relaxation structure beyond local DSMC sampling scatter. Rarefied bow-shock inflation should therefore be viewed, for the present gases and parameter ranges, as a coupled compression–relaxation process in which density collapse and thermal/internal-energy relaxation obey different attached-layer structures, rather than as a universal single-scale rescaling of a continuum-like shock.

For modelling, the results suggest that one-coordinate reduced descriptions are likely to be most effective for density compression. They should not be expected to transfer unchanged to Mach number or translational/rotational temperature, for which additional modes, variable-specific relaxation information, or additional coordinates may be needed.

## Funding

This research received no specific grant from any funding agency, commercial or not-for-profit sectors.

## Declaration of interests

The authors report no conflict of interest.

## Data availability statement

The DSMC-derived post-processing data, ray-registered modal matrices, figure-generation scripts and sensitivity-analysis scripts are available upon reasonable request from the corresponding author.

## Author contributions

E.R. and A.S.S. contributed equally to the development of the code, simulation runs, data analysis, and manuscript preparation.

## A Extraction-choice robustness

The main analysis uses one fixed post-processing pipeline so that all variables are treated consistently. The sensitivity analysis repeats the same extraction with controlled changes in the angular sector, number of body-normal rays, attached-grid resolution, display-independent smoothing width and common-support threshold. This check is designed to separate physically organized modal differences from changes introduced by reasonable numerical registration choices within the same maximum-density-gradient definition used in the main text. In particular, it tracks the leading POD energies of the registered fields under the same alternatives. Table 4 reports the resulting ranges for the nitrogen Knudsen-number sweep. The small spread of the density values and the persistent separation between density and thermal/internal-energy variables support the comparative interpretation used in the main text.

The density field remains nearly rank one for every tested extraction choice within the main maximum-gradient registration, with  $E_1$  confined to 0.985–0.988 and  $C_2$  to 0.996–0.997. By contrast, the Mach-number and thermal/internal-energy fields remain less compact. The absolute modal energies move within

Table 4: Robustness of shock-attached POD compactness to extraction choices for the nitrogen Knudsen-number sweep. The ranges are taken over the tested angular-sector, ray-resolution, attached-grid, smoothing and common-support variants while retaining the maximum-density-gradient marker used in the main analysis. They are sensitivity ranges for the chosen attached-coordinate representation, not physical energy uncertainties.

Variable	Range of $E_1$	Range of $C_2$	Modes for 95%
$\rho$	0.985–0.988	0.996–0.997	1
$M$	0.563–0.632	0.794–0.870	4
$p$	0.790–0.827	0.966–0.974	2
$T_{tr}$	0.865–0.903	0.937–0.950	2–3
$T_{rot}$	0.813–0.887	0.945–0.976	2–3

Table 5: Effect of deliberately changing the compression-layer marker on the nitrogen Knudsen-number POD compactness. The first data column gives the range from table 4 for the main maximum-gradient registration. The last two columns are alternative-registration diagnostics, not uncertainty intervals on the main values. Each entry reports  $E_1/C_2$ .

Variable	Max-gradient range	Half-jump marker	Gradient-centroid marker
$\rho$	0.985–0.988 / 0.996–0.997	0.618 / 0.876	0.913 / 0.963
$M$	0.563–0.632 / 0.794–0.870	0.598 / 0.813	0.601 / 0.808
$p$	0.790–0.827 / 0.966–0.974	0.572 / 0.870	0.807 / 0.927
$T_{tr}$	0.865–0.903 / 0.937–0.950	0.709 / 0.877	0.696 / 0.886
$T_{rot}$	0.813–0.887 / 0.945–0.976	0.853 / 0.927	0.712 / 0.938

the reported ranges, but the ordering of compactness is unchanged: density is the most compact registered field, pressure is moderately compact, and Mach number and thermal variables retain additional coherent modal content. Thus the main conclusion does not rely on a single choice of angular sector, ray resolution, attached-grid size, smoothing width or common-support threshold.

As a separate check, the density-gradient marker was deliberately replaced by broader compression-layer markers: a 50% transition centre with a 10–90 transition width and a gradient-weighted centroid with a gradient-weighted width. These alternatives do not define the same attached coordinate as the main analysis and are therefore not used as uncertainties on the main POD energies. They instead quantify how strongly the modal compactness depends on using a coordinate tied to the sharpest density-gradient ridge rather than to a broader transition centre. Table 5 shows that the numerical energies can change substantially under these alternative registrations, especially for the density and temperature fields. This is expected because the half-jump and centroid coordinates align the broad transition rather than the local compression ridge. Nevertheless, the alternative-marker test does not convert the Mach-number or thermal fields into single-mode registered families; these variables continue to require additional modes. The comparison therefore supports the operational interpretation used throughout the paper: the maximum-gradient coordinate is a reproducible density compression-layer coordinate, and the modal energies should be interpreted within that specified representation.

Empirical diagnostic scaling of extracted shock-layer metrics

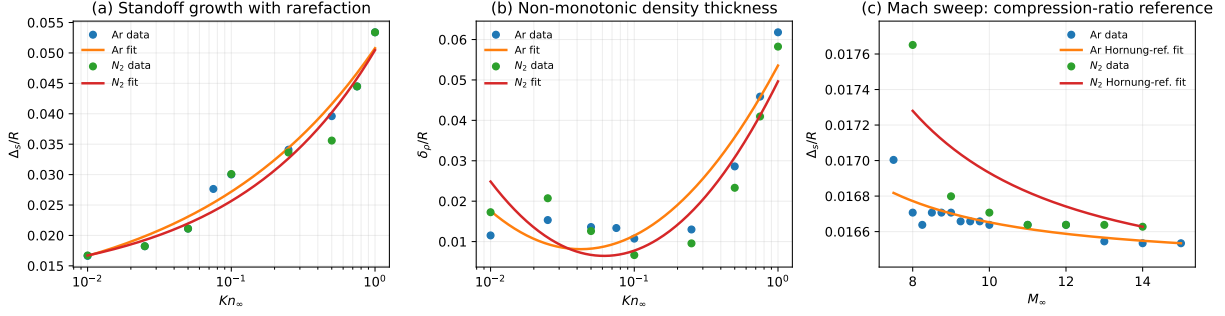


Figure 13: Empirical diagnostic scaling of the extracted shock-layer metrics. Panel (a) shows the monotonic increase of the density-front standoff with  $Kn_\infty$ , summarized by anchored power-law fits. Panel (b) shows the non-monotonic density-thickness trend, summarized by a quadratic fit in  $\log_{10} Kn_\infty$ . Panel (c) shows the Mach-sweep standoff against  $M_\infty$ , with fitted curves based on a Hornung-type compression-ratio reference scale. The curves are compact empirical summaries of the DSMC trends and are not universal analytical correlations. An automatically flagged same-gas Mach-sweep extraction point was excluded from the plotted and fitted Mach-sweep data after inspection.

## B Empirical scaling, uncertainty and finite-snapshot diagnostics

This appendix collects the support diagnostics that are first invoked in the main text after the extraction-choice robustness check. The subsections are ordered by their first use in the article: empirical scaling of the extracted metrics, leave-one-out POD stability, leave-one-out reconstruction, modal coefficient/inner-product/window checks, and finally the representative block-based intervals available for a limited subset of cases. The empirical curves are diagnostic summaries of the extracted DSMC trends, not universal analytical correlations, and the uncertainty intervals are representative sampling-variability checks rather than a new solver-verification exercise.

### B.1 Empirical diagnostic scaling of the extracted metrics

Figure 13 summarizes the extracted standoff and density-thickness metrics using compact empirical fits. The fits are not proposed as analytical shock laws. Panel (a) shows that the density-front standoff increases monotonically with  $Kn_\infty$  for both gases, consistent with a mean-free-path-controlled displacement of the strongest compression region. Panel (b) summarizes the non-monotonic density-thickness trend: the intermediate- $Kn_\infty$  minimum reflects competition between the decreasing sampled density jump and the loss of collisional localization. Panel (c) plots the Mach-sweep standoff against  $M_\infty$ , using a Hornung-type compression-ratio factor only as a low-rarefaction reference scale. One same-gas Mach-sweep extraction point was automatically flagged as an extreme outlier and excluded from the displayed and fitted Mach-sweep data; the fit is therefore used only as a diagnostic summary of the remaining trend.

### B.2 Leave-one-out POD stability

The Knudsen-number POD uses a finite set of eight parameter snapshots. To check whether the compactness ordering is controlled by one individual snapshot, table 6 reports leave-one-out ranges obtained by omitting each snapshot in turn. The density field remains highly stable: the leading-mode energy stays between 0.983 and 0.987 and the leading-mode shape similarity remains above 0.995. Pressure also remains comparatively stable and two-mode compact. Mach number remains less compact for every leave-one-out subset. The

Table 6: Leave-one-out stability of shock-attached POD compactness for the nitrogen Knudsen-number sweep. Each range is obtained by omitting one Knudsen-number snapshot at a time. The mode-shape similarity is the absolute inner product between the baseline and leave-one-out leading modes on their common support.

Variable	Leave-one-out $E_1$ range	Leave-one-out $C_2$ range	Leading-mode similarity range
$\rho$	0.983–0.987	0.993–0.997	0.995–1.000
$M$	0.506–0.686	0.786–0.861	0.961–0.997
$p$	0.717–0.830	0.958–0.979	0.986–1.000
$T_{tr}$	0.449–0.926	0.753–0.967	0.485–1.000
$T_{rot}$	0.589–0.911	0.876–0.981	0.980–1.000

Table 7: Leave-one-out POD reconstruction errors for the nitrogen Knudsen-number sweep. For each left-out snapshot, the POD basis is formed from the remaining snapshots only, and the excluded snapshot is reconstructed with the first  $r$  modes. Values are median relative  $L_2$  errors over the left-out cases, with the 10–90 percentile range in parentheses.

Variable	$r = 1$	$r = 2$	$r = 3$
$\rho$	0.121 (0.0926–0.314)	0.116 (0.0779–0.177)	0.0968 (0.0596–0.145)
$M$	0.402 (0.278–0.588)	0.366 (0.222–0.554)	0.222 (0.132–0.496)
$p$	0.337 (0.191–0.389)	0.176 (0.160–0.231)	0.168 (0.156–0.225)
$T_{tr}$	0.121 (0.0945–0.565)	0.114 (0.0826–0.551)	0.103 (0.0752–0.547)
$T_{rot}$	0.129 (0.0895–0.211)	0.0923 (0.0492–0.136)	0.0798 (0.0471–0.128)

thermal fields show larger variation, particularly  $T_{tr}$ , which is sensitive to removal of the lowest-  $Kn_\infty$  snapshot. This sensitivity is consistent with the physical interpretation in the main text: thermal relaxation is not represented by one universal registered template, and only the organized leading patterns are interpreted.

### B.3 Leave-one-out POD reconstruction

The stability ranges above show how the singular values and leading modes change when one snapshot is removed. A stricter test is to exclude one snapshot, build the POD basis from the remaining snapshots only, and reconstruct the excluded field using the first  $r$  modes. Table 7 and figure 14 report this leave-one-out reconstruction test for the nitrogen Knudsen-number sweep. The test should not be read as a full predictive surrogate validation, because only eight parameter states are available. It is instead a compact check that the modal compactness has reconstruction consequences for unseen points within the sampled sweep.

The results are consistent with the selective-compactness interpretation rather than with a uniformly low-dimensional representation of all variables. Density has a low one-mode median reconstruction error and improves steadily as more modes are retained. Mach number is the hardest field to reconstruct, retaining substantially larger errors even with several modes, which is consistent with its low  $E_1$  and with the fact that density registration does not align velocity deceleration and sound-speed variation simultaneously. The pressure and rotational-temperature fields improve strongly when a second mode is included, whereas  $T_{tr}$  retains a broad high-error tail for some left-out cases. This behaviour supports the interpretation that translational thermal relaxation is not represented by a single density-attached template.

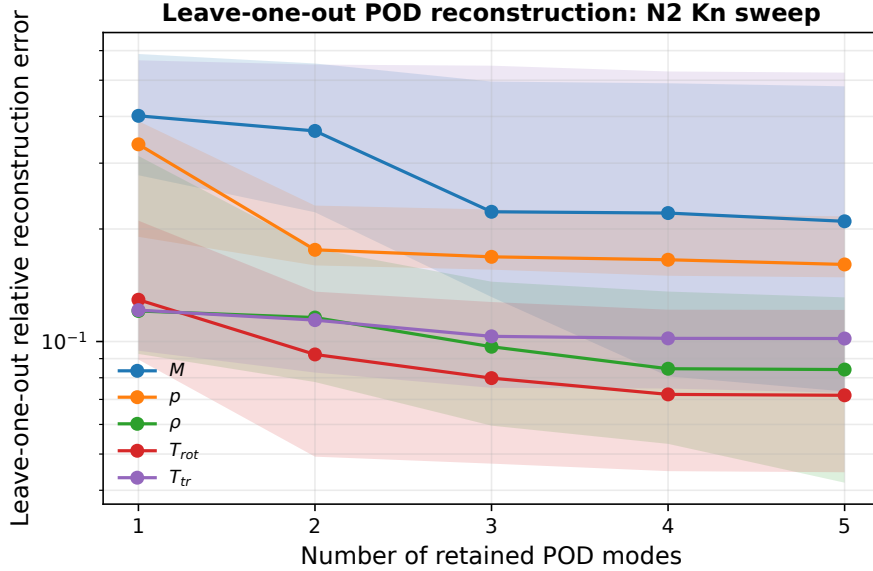


Figure 14: Leave-one-out reconstruction error for the nitrogen Knudsen-number sweep. Each snapshot is excluded in turn, the POD basis is computed from the remaining snapshots, and the excluded field is reconstructed with the first  $r$  modes. The solid curves show median relative  $L_2$  error and the shaded bands show the 10–90 percentile range across left-out cases. The density, pressure and rotational-temperature fields benefit rapidly from the first few modes, whereas Mach number and  $T_{tr}$  retain larger errors for some excluded states. The result supports a selective, rather than universal, low-dimensional attached representation.

#### B.4 POD coefficient, weighting and attached-window sensitivity

The leave-one-out analysis tests whether the finite snapshot set controls the POD energies. A complementary question is whether the modal interpretation depends on the particular Euclidean norm or on the far tails of the attached-coordinate window. Figure 15 therefore reports the first three POD coefficients for the nitrogen Knudsen-number sweep. The coefficients are normalized separately in each panel for visual comparison and are plotted only as parameter-space amplitudes, not as a dynamical modal model. The density and pressure coefficients show that the leading registered modes are engaged coherently as  $Kn_\infty$  is varied, whereas the Mach and thermal coefficients require several comparable modal amplitudes over parts of the sweep. This behaviour is consistent with the energy spectra: density has a nearly one-mode registered representation, while Mach number and the thermal/internal-energy fields retain additional organized directions after density-attached registration.

Table 8 summarizes two further POD sensitivity checks. In the first, the inner product is repeated with moderate coordinate-space weights that emphasize the downstream attached coordinate, the stagnation-side angles or the compression core. In the second, the POD is recomputed on progressively restricted attached-coordinate windows. These are not alternative physical energy norms; they are robustness tests for the compactness ordering. The leading-mode shapes remain very similar to the baseline modes under all tested weights and windows. The density field remains nearly rank one, pressure remains two-mode compact, and the Mach-number field remains the least compact. The translational-temperature field becomes more compact when the downstream attached-coordinate tail is removed, which indicates that part of its additional modal content is carried by the extended relaxation tail. This supports the physical interpretation that thermal relaxation, rather than only density-front displacement, contributes to the similarity breakdown.

POD coefficient evolution across the sweep

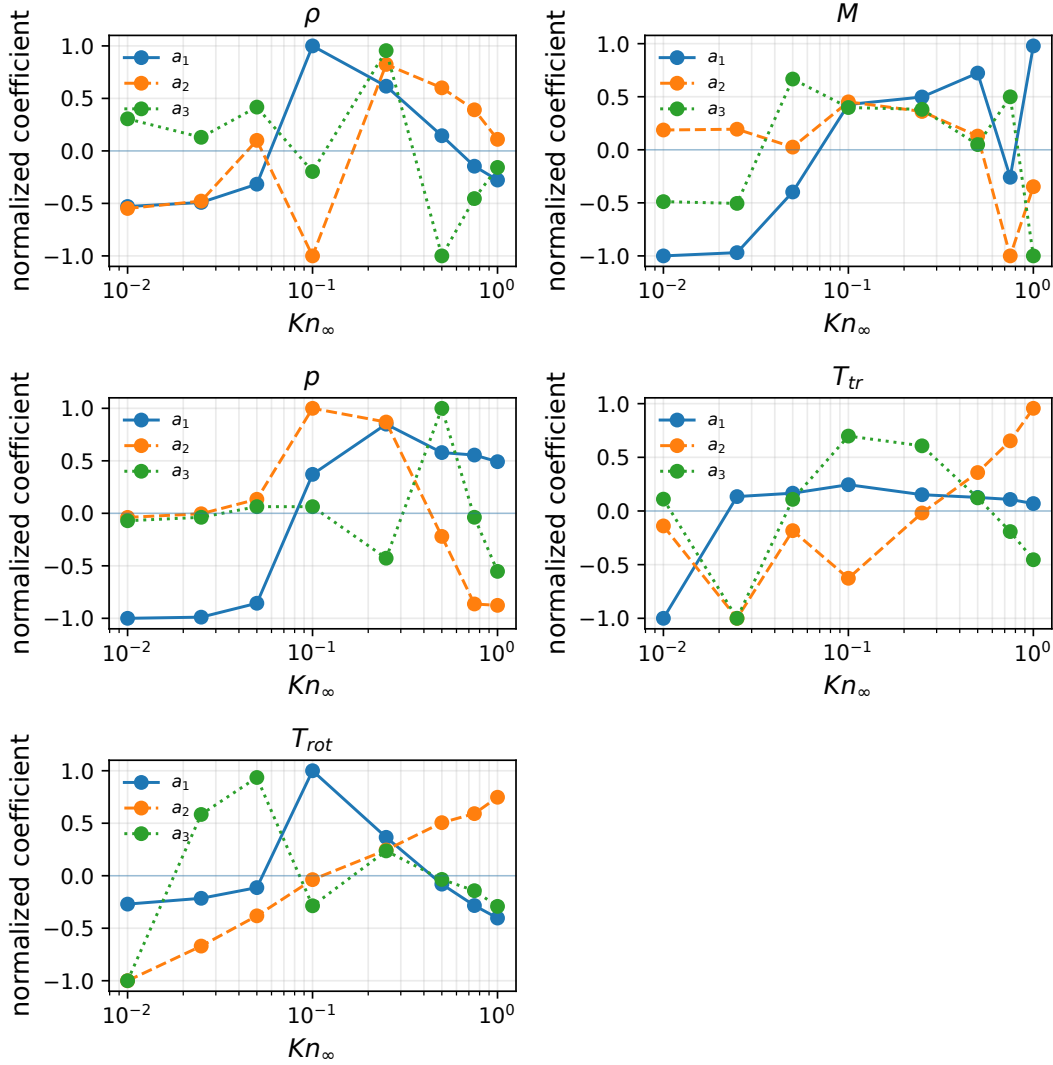


Figure 15: Evolution of the first three POD coefficients for the nitrogen Knudsen-number sweep. The coefficients are normalized within each variable for plotting. The figure is used to show how the leading registered modes are activated across parameter space; it is not a temporal modal analysis and does not assign dynamical frequencies or growth rates. The multi-mode coefficient variation of  $M$ ,  $T_{tr}$  and  $T_{rot}$  is consistent with their slower modal-energy decay in the main text.

Table 8: Compact summary of POD sensitivity to coordinate-space weighting and attached-window restriction for the nitrogen Knudsen-number sweep. The weighting ranges cover uniform, downstream- $\xi$ , stagnation-side- $\theta$  and compression-core weights. The window ranges cover the full  $-1 \leq \xi_q \leq 4$  window and three restricted windows. The similarity column reports the minimum absolute correlation of the leading mode with the corresponding baseline leading mode.

Variable	Weighted inner product				Attached-window restriction			
	$E_1$	$C_2$	$N_{95}$	sim.	$E_1$	$C_2$	$N_{95}$	sim.
$\rho$	0.984–0.985	0.993	1	1.000	0.983–0.984	0.993	1	1.000
$M$	0.539–0.579	0.798–0.809	4	0.994	0.566–0.622	0.786–0.803	4	0.992
$p$	0.767–0.801	0.964–0.972	2	0.997	0.772–0.832	0.966–0.979	2	0.993
$T_{rr}$	0.873–0.888	0.929–0.931	3	1.000	0.878–0.928	0.930–0.961	2–3	1.000
$T_{rot}$	0.831–0.881	0.964–0.968	2	0.998	0.850–0.868	0.964–0.970	2	0.991

Table 9: Representative independent-block intervals for density-based shock-layer metrics. The values are reported as mean  $\pm$  half-width of the nominal 95% interval over the available independent field blocks. Only cases for which such blocks were discoverable in the archived post-processing output are listed.

Gas	Case	$\Delta_s/R$	$\delta_\rho/R$	$\delta_{10-90}/R$
Ar	$Kn_\infty = 0.01, M_\infty = 10$	$0.01665 \pm 0.00013$	$0.0118 \pm 0.0032$	$0.151 \pm 0.379$
$N_2$	$Kn_\infty = 0.01, M_\infty = 9$	$0.01680 \pm 0.00000$	$0.0204 \pm 0.0000$	$0.0892 \pm 0.0000$
$N_2$	$Kn_\infty = 0.01, M_\infty = 10$	$0.01667 \pm 0.00044$	$0.01727 \pm 0.00004$	$0.096 \pm 0.043$

## B.5 Representative block-based intervals

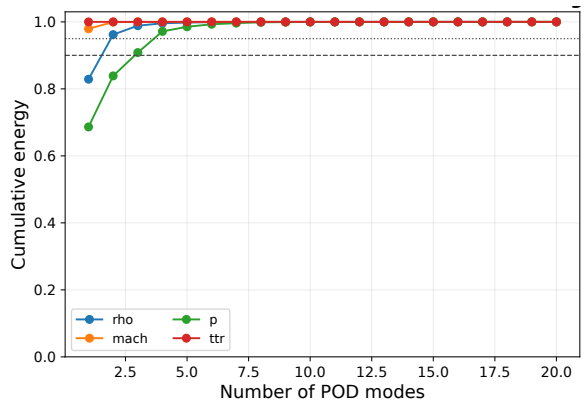
Independent block-averaged fields were available only for a limited subset of cases. Table 9 reports the corresponding intervals for the density-front standoff, gradient thickness and 10–90 transition width. The table is therefore a representative sampling-variability check, not a complete uncertainty quantification for all simulations. The small spread of  $\Delta_s/R$  in the listed cases supports the robustness of the extracted standoff marker in the low-rarefaction regime. The larger spread of the 10–90 width, especially when only two independent blocks are available, indicates that full-transition widths are more sensitive to the diffuse profile tails than the local density-gradient marker.

Because independent time blocks were not available for every case, the main text avoids assigning statistical confidence intervals to all POD energies. The post-processing nevertheless uses medians over the body-normal ray sector, and the robustness checks below vary the extraction choices that most directly affect the registered fields.

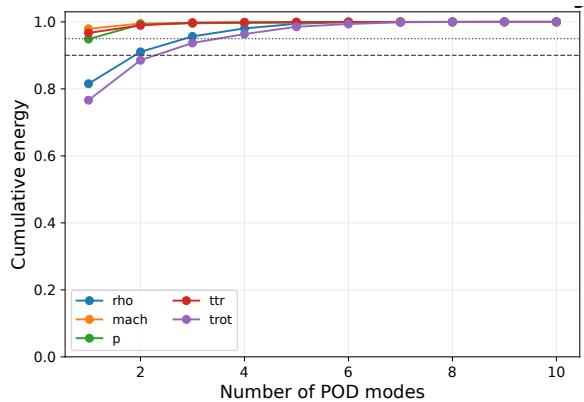
## C Additional modal diagnostics

The main text focuses on the Knudsen-number sweep because rarefaction is the parameter that destroys the unique shock-front representation. The Mach-number sweep provides a useful control case: the shock strength and compression ratio change, but the flow remains at fixed low  $Kn_\infty = 0.01$ , where collisional localization is still strong. The additional modal diagnostics in this appendix therefore check that the conclusions drawn from the Knudsen-number sweep are not simply a consequence of using shock-attached coordinates. They also show which variables remain compact when only the shock strength is varied.

Figure 16 reports the cumulative POD energy for the shock-attached Mach-number sweep. The density



(a) Argon.

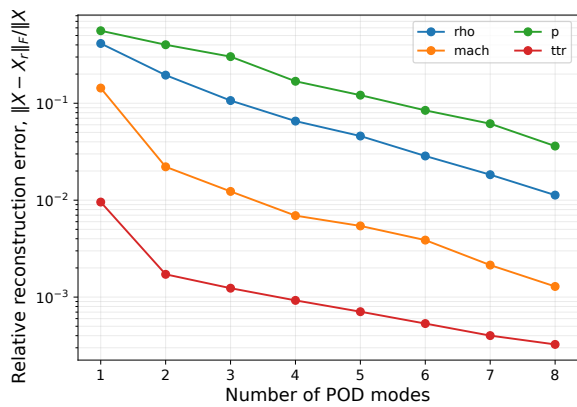


(b) Nitrogen.

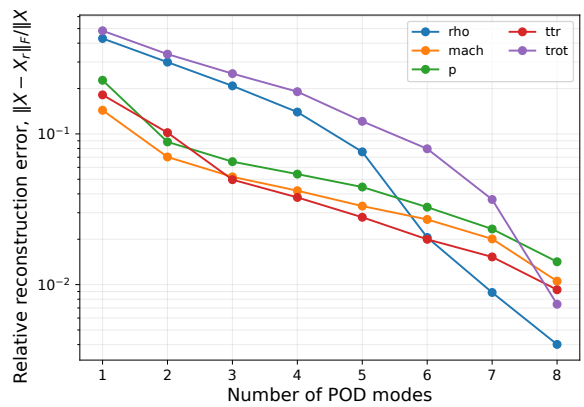
Figure 16: Cumulative POD energy of shock-attached fields in the Mach-number sweep at fixed  $Kn_\infty = 0.01$ . The density field remains compact after registration, confirming that the Mach sweep preserves a coherent compression-layer template. The argon thermal field is also represented by a small number of modes, whereas the nitrogen rotational temperature requires additional modal content because rotational relaxation introduces a thermodynamic scale that is not completely slaved to the density front.

fields remain highly compact after registration, consistent with the density-contour and profile-collapse results in figures 3 and 9. The argon thermal field is also compact, indicating that, for the monatomic gas, changes in Mach number at low rarefaction can be represented largely by a small number of attached-layer structures. Nitrogen is more demanding: the rotational-temperature spectrum decays more slowly, showing that rotational relaxation still introduces a secondary thermodynamic scale even when the density front remains coherent. Thus the Mach sweep is more compact than the Knudsen sweep in the sense of preserving a localized compression layer, but it is not perfectly single-scale for every thermodynamic variable.

Figure 17 gives the corresponding relative reconstruction errors. These curves are a direct accuracy check on the energy spectra in figure 16: a rapid error decay indicates that a small modal basis reconstructs the registered Mach-sweep family, while a slower decay identifies residual variable-specific structure. The density errors fall rapidly for both gases, which reinforces the interpretation that Mach variation at low rarefaction mainly shifts and strengthens a coherent density-compression layer. The slower thermal error decay, especially for nitrogen rotational temperature, is consistent with the main-text conclusion that internal-energy relaxation can retain coherent secondary structure even when the density field is compact. The appendix therefore supports, rather than replaces, the main result: rarefaction is what produces the broad kinetic delocalization, while gas-dependent thermal relaxation controls the remaining modal content after registration.



(a) Argon.



(b) Nitrogen.

Figure 17: Relative reconstruction error for shock-attached fields in the Mach-number sweep at  $Kn_\infty = 0.01$ . The rapid decay of the density error confirms that the registered density-compression layer is compact when Mach number, rather than Knudsen number, is varied. The slower decay of the nitrogen thermal errors indicates residual coherent relaxation structure, consistent with the modal spectra in figure 16 and with the main-text interpretation of thermal/internal-energy similarity breakdown.

## References

- Hassan Akhlaghi, Abbas Daliri, and Mohammad Reza Soltani. Shock-wave-detection technique for high-speed rarefied-gas flows. *AIAA Journal*, 55(11):3747–3756, 2017. doi: 10.2514/1.J055819.
- Hassan Akhlaghi, Ehsan Roohi, Abbas Daliri, and Mohammad-Reza Soltani. Shock polar investigation in supersonic rarefied gas flows over a circular cylinder. *Physics of Fluids*, 33(5):052006, 2021. doi: 10.1063/5.0050571.
- Gal Berkooz, Philip Holmes, and John L. Lumley. The proper orthogonal decomposition in the analysis of turbulent flows. *Annual Review of Fluid Mechanics*, 25:539–575, 1993. doi: 10.1146/annurev.fl.25.010193.002543.
- Graeme A. Bird. *Molecular Gas Dynamics and the Direct Simulation of Gas Flows*. Clarendon Press, Oxford, 1994.
- Carlo Cercignani. *Rarefied Gas Dynamics: From Basic Concepts to Actual Calculations*. Cambridge University Press, 2000.
- Behnam Goshayeshi, Ehsan Roohi, and Stefan Stefanov. A novel simplified Bernoulli trials collision scheme in the direct simulation Monte Carlo with intelligence over particle distances. *Physics of Fluids*, 27(10):107104, 2015a. doi: 10.1063/1.4934588.
- Behnam Goshayeshi, Ehsan Roohi, and Stefan Stefanov. DSMC simulation of hypersonic flows using an improved SBT-TAS technique. *Journal of Computational Physics*, 303:28–44, 2015b. doi: 10.1016/j.jcp.2015.09.044.
- H. G. Hornung. Non-equilibrium dissociating nitrogen flow over spheres and circular cylinders. *Journal of Fluid Mechanics*, 53(1):149–176, 1972. doi: 10.1017/S0022112072000084.
- H. G. Hornung. Shock detachment and drag in hypersonic flow over wedges and circular cylinders. *Journal of Fluid Mechanics*, 915:A100, 2021. doi: 10.1017/jfm.2021.187.
- H. G. Hornung, Jan Martinez Schramm, and Klaus Hannemann. Hypersonic flow over spherically blunted cone capsules for atmospheric entry. part 1. the sharp cone and the sphere. *Journal of Fluid Mechanics*, 871:1097–1116, 2019. doi: 10.1017/jfm.2019.342.
- Jin Huang, Kun Xu, and Pu Yu. A unified gas-kinetic scheme for continuum and rarefied flows ii: Multi-dimensional cases. *Communications in Computational Physics*, 12(3):662–690, 2012. doi: 10.4208/cicp.120211.220911s.
- Yazhong Jiang, Xuxu Sun, Jie Niu, and Jun Zhang. Study of shock-shock interactions in rarefied flows using direct simulation Monte Carlo method. *Aerospace Science and Technology*, 173:111768, 2026. doi: 10.1016/j.ast.2026.111768.
- B. John, X. J. Gu, R. W. Barber, and D. R. Emerson. High-speed rarefied flow past a rotating cylinder: The inverse magnus effect. *AIAA Journal*, 54(2):521–532, 2016.
- B. John, X. J. Gu, and D. R. Emerson. Computation of aerodynamic forces under nonequilibrium conditions: Flow past a spinning cylinder. *AIAA Journal*, 56(1):198–209, 2018.
- B. John, X. J. Gu, R. W. Barber, and D. R. Emerson. Non-equilibrium effects on flow past a circular cylinder in the slip and early transition regime. *Journal of Fluid Mechanics*, 871:626–662, 2019.

- George E. Karniadakis, Ali Beskok, and Narayana Aluru. *Microflows and Nanoflows: Fundamentals and Simulation*. Springer, 2005.
- Irmak T. Karpuzcu, Mert Senkardesler, and Deborah A. Levin. On flow unsteadiness in strongly separated high-speed ramp flows using kinetic and data-driven methods. *Physics of Fluids*, 37(9):096136, 2025. doi: 10.1063/5.0281770.
- Angelos Klothakis, Jr. Quintanilha, Helio, Saurabh S. Sawant, Eftychios Protopapadakis, Vassilis Theofilis, and Deborah A. Levin. Linear stability analysis of hypersonic boundary layers computed by a kinetic approach: A semi-infinite flat plate at Mach 4.5 and 9, 2021.
- Chang Liu, Yajun Zhu, and Kun Xu. Unified gas-kinetic wave-particle methods i: Continuum and rarefied gas flow. *Journal of Computational Physics*, 401:108977, 2020. doi: 10.1016/j.jcp.2019.108977.
- Andrew J. Lofthouse, Iain D. Boyd, and Michael J. Wright. Effects of continuum breakdown on hypersonic aerothermodynamics. *Physics of Fluids*, 19(2):027105, 2007. doi: 10.1063/1.2710289.
- Andrew J. Lofthouse, Leonardo C. Scalabrin, and Iain D. Boyd. Velocity slip and temperature jump in hypersonic aerothermodynamics. *Journal of Thermophysics and Heat Transfer*, 22(1):38–49, 2008. doi: 10.2514/1.31280.
- John L. Lumley. The structure of inhomogeneous turbulent flows. *Atmospheric Turbulence and Radio Wave Propagation*, pages 166–178, 1967.
- Vladimir V. Riabov. Aerodynamics of a spinning cylinder in rarefied gas flows. *Journal of Spacecraft and Rockets*, 36(2):293–298, 1999.
- Ehsan Roohi and Amirmehran Mahdavi. Shock-centered low-rank structure and neural-operator representation of rarefied micro-nozzle flows, 2026.
- Ehsan Roohi, Hassan Akhlaghi, and Stefan Stefanov. *Advances in Direct Simulation Monte Carlo: From Micro-Scale to Rarefied Flow Phenomena*. Springer Nature Singapore, Singapore, 2025. ISBN 978-981-96-8200-3. doi: 10.1007/978-981-96-8200-3.
- Ehsan Roohi, Ahmad Shoja-Sani, and Fahimeh Ebrahimzadeh Azghadi. Neural networks for rarefied gas dynamics: Relaxation problem, polyatomic shock waves, and hypersonic cylinder flow. *Physics of Fluids*, 38:057108, 2026a. doi: 10.1063/5.0334590.
- Ehsan Roohi, Ahmad Shoja-Sani, and Stefan Stefanov. Physics constrained neural collision operators for hard sphere surrogates and ab initio angle prediction in direct simulation monte carlo. *Physics of Fluids*, 38:000000, 2026b. doi: 10.1063/5.0328463.
- Clarence W. Rowley, Igor Mezić, Shervin Bagheri, Philipp Schlatter, and Dan S. Henningson. Spectral analysis of nonlinear flows. *Journal of Fluid Mechanics*, 641:115–127, 2009. doi: 10.1017/S0022112009992059.
- Saurabh S. Sawant, Vassilios Theofilis, and Deborah A. Levin. Kinetic modelling of three-dimensional shock/laminar separation bubble instabilities in hypersonic flows over a double wedge, 2021.
- Peter J. Schmid. Dynamic mode decomposition of numerical and experimental data. *Journal of Fluid Mechanics*, 656:5–28, 2010. doi: 10.1017/S0022112010001217.

- Thomas E. Schwartzentruber, Leonardo C. Scalabrin, and Iain D. Boyd. A modular particle–continuum numerical method for hypersonic non-equilibrium gas flows. *Journal of Computational Physics*, 225(1): 1159–1174, 2007. doi: 10.1016/j.jcp.2007.01.022.
- Mert Senkardesler, Irmak T. Karpuzcu, Deborah A. Levin, and Vassilis Theofilis. A molecular gas dynamics study of hypersonic boundary layer second Mack mode instabilities, 2025.
- Felix Sharipov. Data on the velocity slip and temperature jump on a gas-solid interface. *Journal of Physical and Chemical Reference Data*, 40:023101, 2011. doi: 10.1063/1.3580290.
- Felix Sharipov and Denize Kalempa. Gas flow around a longitudinally moving cylinder in the whole range of the knudsen number. *Journal of Vacuum Science & Technology A*, 21(3):735–745, 2003. doi: 10.1116/1.1560710.
- Lawrence Sirovich. Turbulence and the dynamics of coherent structures. part i: Coherent structures. *Quarterly of Applied Mathematics*, 45(3):561–571, 1987.
- Yoshio Sone. *Molecular Gas Dynamics: Theory, Techniques, and Applications*. Birkhäuser, 2007.
- Stefan K. Stefanov, Iain D. Boyd, and Chunpei Cai. Monte carlo analysis of macroscopic fluctuations in a rarefied hypersonic flow around a cylinder. *Physics of Fluids*, 12(2):487–497, 2000.
- Kunihiko Taira, Steven L. Brunton, Scott T. M. Dawson, Clarence W. Rowley, Tim Colonius, Beverley J. McKeon, Oliver T. Schmidt, Stanislav Gordeyev, Vassilios Theofilis, and Lawrence S. Ukeiley. Modal analysis of fluid flows: An overview. *AIAA Journal*, 55(12):4013–4041, 2017. doi: 10.2514/1.J056060.
- Aaron Towne, Oliver T. Schmidt, and Tim Colonius. Spectral proper orthogonal decomposition and its relationship to dynamic mode decomposition and resolvent analysis. *Journal of Fluid Mechanics*, 847: 821–867, 2018. doi: 10.1017/jfm.2018.283.
- Yajun Zhu, Chengwen Zhong, and Kun Xu. Unified gas-kinetic wave-particle methods. i. continuum and rarefied gas flow. *Journal of Computational Physics*, 383:190–210, 2019. doi: 10.1016/j.jcp.2019.01.023.